Interactions between Cloud Microphysics and Cumulus Convection in a General Circulation Model

LAURA D. FOWLER AND DAVID A. RANDALL

Department of Atmospheric Science, Colorado State University, Fort Collins, Colorado

(Manuscript received 1 May 2001, in final form 17 May 2002)

ABSTRACT

In the Colorado State University general circulation model, cumulus detrainment of cloud water and cloud ice has been, up to now, the only direct coupling between convective and large-scale condensation processes. This one-way interaction from the convective to the large-scale environment parameterizes, in a highly simplified manner, the growth of anvils spreading horizontally at the tops of narrow cumulus updrafts. The reverse interaction from the large-scale to the convective updrafts, through which large-scale cloud water and cloud ice can affect microphysical processes occurring in individual convective updrafts, is missing. In addition, the effects of compensating subsidence on cloud water and cloud ice are not taken into account.

A new parameterization of convection, called ''EAUCUP,'' has been developed, in which large-scale water vapor, cloud water, and cloud ice are allowed to enter the sides of the convective updrafts and can be lifted to the tops of the clouds. As the various water species are lifted, cloud microphysical processes take place, removing excess cloud water and cloud ice in the form of rain and snow. The partitioning of condensed vapor between cloud water and cloud ice, and between rain and snow, is based on temperature. The effects of compensating subsidence on the large-scale water vapor, cloud water, and cloud ice are computed separately. Convective rain is assumed to fall instantaneously to the surface. Three treatments of the convective snow are tested: 1) assuming that all snow is detrained at the tops of convective updrafts, 2) assuming that all snow falls outside of the updrafts and may evaporate, and 3) assuming that snow falls entirely inside the updrafts and melts to form rain.

Including entrainment of large-scale cloud water and cloud ice inside the updrafts, large-scale compensating subsidence unifies the parameterizations of large-scale cloud microphysics and convection, but have a lesser impact than the treatment of convective snow on the simulated climate. Differences between the three alternate treatments of convective snow are discussed. Emphasis is on the change in the convective, large-scale, and radiative tendencies of temperature, and change in the convective and large-scale tendencies of water vapor, cloud water, cloud ice, and snow. Below the stratiform anvils, the change in latent heating due to the change in both convective and large-scale heatings contributes a major part to the differences in diabatic heating among the three simulations. Above the stratiform anvils, differences in the diabatic heating between the three simulations result primarily because of differences in the longwave radiative cooling. In particular, detraining convective snow at the tops of convective updrafts yields a strong increase in the longwave radiative cooling associated with increased upper-tropospheric cloudiness. The simulated climate is wetter and colder when convective snow is detrained at the tops of the updrafts than when it is detrained on the sides of the updrafts or when it falls entirely inside the updrafts. This result highlights the importance of the treatment of the ice phase and associated precipitation in the convective cloud models used in cumulus parameterizations.

1. Introduction

In the last decade, parameterizations of moist processes in general circulation models (GCMs) have focused on developing realistic interactions between the convective and stratiform clouds. The surge of prognostic equations to describe the spatial and temporal evolution of water vapor and condensates (Tiedtke 1993; Del Genio 1996; Fowler et al. 1996; Rotstayn 1997; Rasch and Kristjansson 1998; Sud and Walker 1999a) permitted parameterizations of convection to explicitly represent the formation of clouds by convection. Tiedtke (1993) wrote that ''the representation of cloud formation by convection is rather straightforward if cumulus convection is parameterized by means of a mass-flux scheme, because the source terms for the cloud fields can be readily expressed in terms of available model parameters.'' Specifically, convective detrainment of cloud water and cloud ice acts as a source of large-scale cloud water and cloud ice to simulate the growth of extended anvils at the tops of the narrow convective updrafts. Except for Sud and Walker (1999a,b), Jakob (2000), and this study, the reverse interaction from the large-scale to the convective environment, through which large-scale cloud water and cloud ice can modify microphysical processes occurring

Corresponding author address: Dr. Laura D. Fowler, Department of Atmospheric Science, Colorado State University, Fort Collins, CO 80523.
E-mail: laura@atmos.colostate.edu

in individual convective updrafts, has not been addressed.

The convective parameterization of Arakawa and Schubert (1974, hereafter AS74) based on the discretization of a cumulus ensemble into subensembles according to the fractional entrainment rate, used a simple cloud model that, in particular, neglected to take into account the ice phase. Using a simple cloud model to parameterize cloud microphysical and precipitation processes occurring in individual convective updrafts comes at the expense of omitting all details of the formation mechanisms of detrained cloud water and cloud ice, and convective precipitation inside the convective updraft. The AS74 budget equations for an individual cloud were limited to those of mass, static energy, water vapor, and liquid water. Detrained liquid water immediately evaporated at the top of the updraft. AS74 prescribed convective precipitation as a fraction of the liquid water formed in the updraft, and assumed that precipitation fell instantaneously to the surface. Lord (1978) revised the AS74 cloud model, and included a budget equation for ice. As liquid water, convective ice immediately evaporated at cloud top. As in AS74, convective precipitation was prescribed, and immediately removed from the atmosphere. The AS74-based parameterization of convection (Ding and Randall 1998; Pan and Randall 1998) developed for the Colorado State University (CSU) general circulation model uses modified versions of Lord's (1978) cloud model. Detrained cloud water and cloud ice are used as large-scale sources of cloud water and cloud ice, respectively (Fowler et al. 1996).

Emanuel and Pierrehumbert (1996), and later, Emanuel and Zivkovic-Rothman (1999) demonstrate that ''atmospheric water vapor content depends strongly on microphysical processes within convective and associated stratiform clouds, and on the evaporation of precipitation.'' Both argue, however, that ''little attention has been paid to microphysical aspects of convective parameterizations used in climate models.'' Earlier, Renno et al. (1994) showed that the climate equilibrium of a one-dimensional radiative convective model was highly sensitive to the moisture profiles calculated with various cumulus convective schemes. They found that clouds with high precipitation efficiency produced cold and dry climates while clouds with low precipitation efficiency led to moist and warm climates.

As stated above, in the AS74 and later AS74-based parameterizations of convection developed for the CSU GCM, convective rain starts in the warm part of the updraft only, and is crudely defined as a fraction of the condensed water. Furthermore, convective rain is instantaneously removed from the atmosphere. No convective rain initiates from the cold section of the updraft. Our long-term objective is to develop a physically based parameterization of convective precipitation that includes initiation of falling rain and snow from both the warm and cold sections of the updraft, and realistic conversion processes of cloud water to rain, and cloud ice to snow. We also plan to move away from the assumption that rain falls instantaneously to the surface by explicitly calculating the vertical velocity of the convective updraft and the terminal velocities of rain and snow, as in Cheng and Arakawa (1997), Sud and Walker (1999a), and Donner et al. (2000). The goal of this particular study is to take a first step in describing convective and large-scale cloud microphysical and precipitation processes with a single parameterization while more realistically parameterizing interactions between the convective and stratiform clouds. We focus on the sensitivity of the CSU CGM when convective snow is allowed to form in the cold section of the cumulus cloud. Our revised AS74-based cloud model and revised feedbacks on the large-scale circulation will be referred to as ''EAUCUP.'' Figure 1 illustrates how interactions between convective and stratiform condensation processes are parameterized in the CSU GCM. Because the GCM does not include a parameterization of fractional cloudiness at this time, we assume that, once formed, a large-scale cloud occupies the entire area of the model grid box.

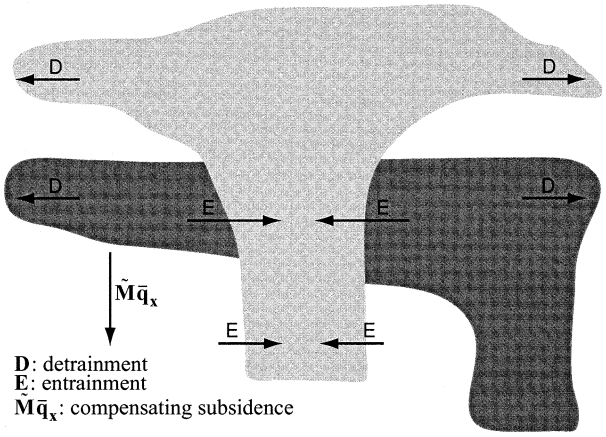

FIG. 1. Schematic illustration of the different interactions between the convective and large-scale environments. Anvils occupy the total horizontal area of the GCM grid box.

Figure 1 shows two large-scale clouds formed by detrainment at the tops of two narrower convective updrafts. Each cloud is assumed to have a horizontal fractional area equal to 1. We show the convective updrafts starting at two different levels. Here, E represents the rate of mass entrainment from the cloudy or cloud-free large-scale environment into a convective updraft. If the large-scale environment is cloud free, only large-scale moist static energy and water vapor are entrained into the updraft. This is the case for the light gray cloud at the base of the convective updraft. If the large-scale environment is cloudy, large-scale moist static energy, water vapor, cloud water, and cloud ice are entrained into the updraft. This is the case for the light gray cloud when its convective updraft grows through the anvil of

the dark gray cloud. Next, D represents the detrainment of mass at the tops of the convective updrafts. As mentioned earlier, detrained cloud water and cloud ice act as sources of cloud water and cloud ice for our parameterization of large-scale cloud microphysics (later referred to as EAULIQ; Fowler et al. 1996). The direct effect of letting large-scale cloud water and cloud ice enter the sides of the convective updrafts is to enhance the production of convective precipitation and detrained cloud water and cloud ice at cloud tops. Finally, in Fig. 1, $\tilde{M}\overline{q}_x$ where $\tilde{M}$ is the downward mass flux between clouds, is the compensating subsidence of $\overline{q}_x$. Here, $\overline{q}_x$ may represent the large-scale moist static energy, water vapor, cloud water, and cloud ice between the convective updrafts.

In section 2, we outline the characteristics of the EAUCUP version of the AS74 parameterization of convection while details of the convective cloud model are provided in section 3. Section 4 describes the designs of three sensitivity experiments aimed at understanding how the treatment of snow in convective updrafts affects convective and large-scale moist processes. Differences in the convective and large-scale tendencies of temperature and water species among the three simulations are discussed in sections 5 and 6, respectively. Section 7 focuses on the response of the atmospheric general circulation. Finally, section 8 summarizes our findings and outlines the chief differences found between EAUCUP and the cumulus parameterization previously used in the CSU GCM.

2. Large-scale budget equations

Let $\overline{q}_v$, $\overline{q}_c$, $\overline{q}_i$, $\overline{q}_r$, and $\overline{q}_s$ be the large-scale water vapor, cloud water, cloud ice, rain, and snow mixing ratios, respectively; let $\overline{s}$ be the large-scale dry static energy. The continuity equations on a σ surface for $\overline{q}_v$, $\overline{q}_c$, $\overline{q}_i$, $\overline{q}_r$, $\overline{q}_s$, and $\overline{s}$ due to convective, large-scale condensation, and radiative processes can be written as

$$\frac{\partial}{\partial t}(\pi^*\overline{q}_x) + \nabla\cdot(\pi^*\mathbf{V}\overline{q}_x) + \frac{\partial}{\partial\sigma}(\pi^*\dot{\sigma}\overline{q}_x) = \mathrm{SCUP}_x + g\frac{\partial}{\partial\sigma}\rho\overline{w'q_x'} + \mathrm{SLSP}_x, \quad (1)$$

where x refers to the subscripts v for water vapor, c for cloud water, i for cloud ice, r for rain, and s for snow, and

$$\frac{\partial}{\partial t}(\pi^*\overline{s}) + \nabla\cdot(\pi^*\mathbf{V}\overline{s}) + \frac{\partial}{\partial\sigma}(\pi^*\dot{\sigma}\overline{s}) = \mathrm{SCUP}_T + g\frac{\partial}{\partial\sigma}\rho\overline{w's'} + \mathrm{SLSP}_T + \mathrm{SRAD}_T. \quad (2)$$

In Eqs. (1) and (2), $\nabla\cdot(\,)$ denotes the divergence operator on a σ surface, π^* is the pressure scale used with the definition of σ (see Suarez et al. 1983), $\mathbf{V}$ is the horizontal wind vector, and $\dot{\sigma}$ is the large-scale vertical velocity. On the right-hand side of Eqs. (1) and (2), the terms SCUP_x and SCUP_T (where subscript T refers to temperature) represent the rates of change of $\overline{q}_x$ and $\overline{s}$ due to microphysical processes occurring in the convective updrafts, while the terms $(\partial/\partial\sigma)\rho\overline{w'q_x'}$ and $(\partial/\partial\sigma)\rho\overline{w's'}$ represent the vertical transports of $\overline{q}_x$ and $\overline{s}$ by the convective circulations. The terms SCUP_x and SCUP_T will be discussed in section 3, where microphysical processes occurring in the convective updrafts are described. SLSP_x and SLSP_T are the tendencies of $\overline{q}_x$ and $\overline{s}$, due to large-scale condensation processes, and SRAD_T is the tendency of $\overline{s}$ due to long- and shortwave radiative processes.

As discussed by AS74, the eddy vertical transport of dry static energy and individual water species of a cumulus ensemble can be expressed, for a single cloud type, as

$$\rho\overline{w's'} = M_c(s_c - \overline{s}), \quad \text{and} \quad (3)$$

$$\rho\overline{w'q_x'} = M_c(q_{xc} - \overline{q}_x). \quad (4)$$

In Eqs. (3) and (4), M_c is the convective mass flux; s_c is the in-cloud dry static energy; and q_{xc} is the in-cloud water vapor, cloud water, cloud ice, rain, or snow mixing ratio. Looking at Eqs. (1) and (2), the tendencies of $\overline{q}_v$, $\overline{q}_c$, $\overline{q}_i$, $\overline{q}_r$, $\overline{q}_s$, and $\overline{s}$ due to convection can be determined once the vertical distribution of the convective mass flux, and the in-cloud vertical profiles of temperature, cloud water, cloud ice, rain, and snow have been calculated.

The parameterization of cumulus convection previously used in the CSU GCM is based on AS74 and includes the ice phase following Lord (1978). In recent years, two major modifications were made.

First, the assumption of strict quasi equilibrium of the cloud work function $A(\lambda)$ was replaced by a prognostic closure through the introduction of a prognostic equation for the vertically integrated cumulus kinetic energy of each cloud type (Pan 1995; Pan and Randall 1998):

$$\frac{d}{dt}K(\lambda) = M_B(\lambda)A(\lambda) - \frac{K(\lambda)}{\tau_D(\lambda)}. \quad (5)$$

Here, λ is the fractional entrainment rate, $K(\lambda)$ is the vertically integrated cumulus kinetic energy, $M_B(\lambda)$ is the cloud-base mass flux, and $\tau_D(\lambda)$ is a dissipation timescale. It is also assumed that

$$K(\lambda) = \alpha M_B^2(\lambda), \quad (6)$$

where α is a ''conversion factor'' (Arakawa and Xu 1992) relating the cumulus mass flux to the cumulus kinetic energy. Although α has dimensions of length^4 mass^{-1}, and depends on the depth of the cloud, the strength of the convective activity, and the vertical shear of the horizontal wind (Pan and Randall 1998; Lin et al. 2000), in the present study α is treated as a constant equal to 1×10^8 m^4 kg^{-1}.

Second, the exponential profile of the normalized

mass flux $\eta(\lambda)$ used in AS74 was replaced by a linear profile:

$$\eta(z, \lambda) = 1 + \lambda(z - z_B) + (\Delta\eta)_{\text{TOP}} \quad \text{for } z_B \le z \le z_D(\lambda), \tag{7}$$

where z is a given height inside the cumulus updraft, z_B is the cloud-base height, $z_D(\lambda)$ is the detrainment level of an individual cumulus ensemble, and $(\Delta\eta)_{\text{TOP}}$ is the amount of entrainment at cloud top (Cheng and Arakawa 1997). A linear increase of the normalized mass flux with the height of the mass entrainment was first proposed by Moorthi and Suarez (1992), and has also been used by Sud and Walker (1999a,b). Finally, convection is not restricted to start at the top of the planetary boundary layer (PBL), but may also start at any level in the free troposphere (Ding 1995; Ding and Randall 1998).

Eqs. (5) and (6) are solved to derive the cloud-base mass flux of individual cloud ensembles. The convective mass flux $M_c(\lambda)$ is then obtained using Eq. (7) and the relationship

$$M_c(z, \lambda) = \eta(z, \lambda)M_B(\lambda). \tag{8}$$

3. Cumulus cloud model

The EAUCUP cumulus cloud model differs significantly from that of Lord (1978). Lord (1978) assumes that, for each cloud type, the flux convergence of total water (water vapor plus cloud water plus cloud ice) depends on the entrainment of total water from the large-scale environment, on the detrainment of total water at the top of the convective updraft, and on the production of precipitation. Because Lord (1978) assumes that large-scale cloud water and cloud ice are equal to zero, the entrainment of total water from the large-scale environment reduces to that of water vapor, and the cloud water and cloud ice detrained at the top of the cloud are immediately evaporated. Lord (1978) assumes that a fraction of the liquid water formed in the convective updrafts is supercooled so that it can enhance the production of cloud ice. The fraction of supercooled water depends on the in-cloud temperature and the amount of liquid water in the cloud. A fraction of the remaining cloud water is converted to precipitation, which falls instantaneously to the ground.

The coexistence of EAUCUP and EAULIQ enables us to entrain, not only large-scale water vapor, but also large-scale cloud water and cloud ice into the convective updraft. It also allows us to detrain not only convective water vapor, but also convective cloud water and cloud ice to form large-scale anvils (Fowler et al. 1996; Fowler and Randall 1996). As water vapor, cloud water, and cloud ice are lifted to the tops of the clouds, microphysical processes take place. In particular, excess cloud water and cloud ice are removed in the forms of convective rain and convective snow. In contrast to Lord (1978), who considers only one kind of precipitation, EAUCUP permits a fraction of the in-cloud ice content to precipitate in the form of convective snow. We calculate separately the vertical profiles of water vapor, cloud water, and cloud ice, using

$$\frac{\partial}{\partial z}[\eta(z, \lambda)q_{xc}] = \lambda\overline{q}_x + \text{CUP}_{xc}, \tag{9}$$

where $\overline{q}_x$, q_{xc}, and $\eta(\lambda)$ were defined in Eqs. (1), (4), and (7), respectively. In Eq. (9), CUP_{xc} is a symbolic term that represents the change in q_{xc} due to cloud microphysics occurring in the updrafts. In doing so, we separately determine the individual vertical profiles of q_{vc}, q_{cc}, and q_{ic}.

In Eq. (2), the dry static energy $\overline{s}$ is defined as

$$\overline{s} = c_p\overline{T} + gz, \tag{10}$$

where $\overline{T}$ is the large-scale temperature, gz is the geopotential height, and c_p is the specific humidity of dry air. Let us denote by $\overline{s}_v$ and $\overline{h}$, the large-scale virtual static energy and generalized moist static energy, respectively. Here, $\overline{s}_v$ and $\overline{h}$ are defined as

$$\overline{s}_v \equiv s + c_p\overline{T}(0.608\overline{q}_v - \overline{q}_c - \overline{q}_r - \overline{q}_i - \overline{q}_s), \tag{11}$$

where $\overline{s}_v$ includes the loading of condensed water in the form of cloud water, cloud ice, rain, or snow, and

$$\overline{h} \equiv \overline{s} + L_c q_v - L_f(q_i + q_s), \tag{12}$$

where L_c and L_f are the latent heats of condensation and latent heat of fusion, respectively.

Let us also define $\overline{h}_s$ and $\overline{q}_{vs}$ as the large-scale saturation moist static energy and saturation mixing ratio. Here, $\overline{h}_s$ is defined as

$$\overline{h}_s = c_p\overline{T} + L\overline{q}_{vs}. \tag{13}$$

In Eq. (13), $\overline{q}_{vs}$ is the saturation mixing ratio with respect to water when $\overline{T} \ge 0°\text{C}$ and with respect to ice when $-20°\text{C} < \overline{T}$. In the temperature range $-20°\text{C} \le \overline{T} < 0°\text{C}$, the saturation vapor pressure $e_s(\overline{T})$ is obtained by linear interpolation between the saturation vapor pressures with respect to water and ice; $\overline{q}_{vs}$ is then computed using $e_s(\overline{T})$, and L is equal to L_c when $\overline{T} \ge 0°\text{C}$ and equal to the latent heat of sublimation L_s when $-20°\text{C} < \overline{T}$. When $-20°\text{C} \le \overline{T} < 0°\text{C}$, L is interpolated linearly as a function of L_c and L_s. These temperature thresholds, which specify the width of the temperature window in which supercooled cloud water and cloud ice are allowed to coexist are, for consistency, the same ones used in our parameterization of large-scale cloud microphysical processes, as described in Fowler et al. (1996).

Let us denote by h_c the in-cloud generalized moist static energy, and let q_{vc}, q_{cc}, q_{rc}, q_{ic}, and q_{sc} in a layer k and a cloud type i be also defined as in Lord et al. (1982, refer to their appendix); let $[k + 1/2, i]$ be the indices of h_c, q_{vc}, q_{cc}, q_{rc}, q_{ic}, and q_{sc} entering the layer k from below, $[k, i]$ be their indices after lifting but before precipitation processes occur, and $[k - 1/2, i]$ be their indices after precipitation processes and leaving layer k, as in the schematic diagram shown in Fig. 2.

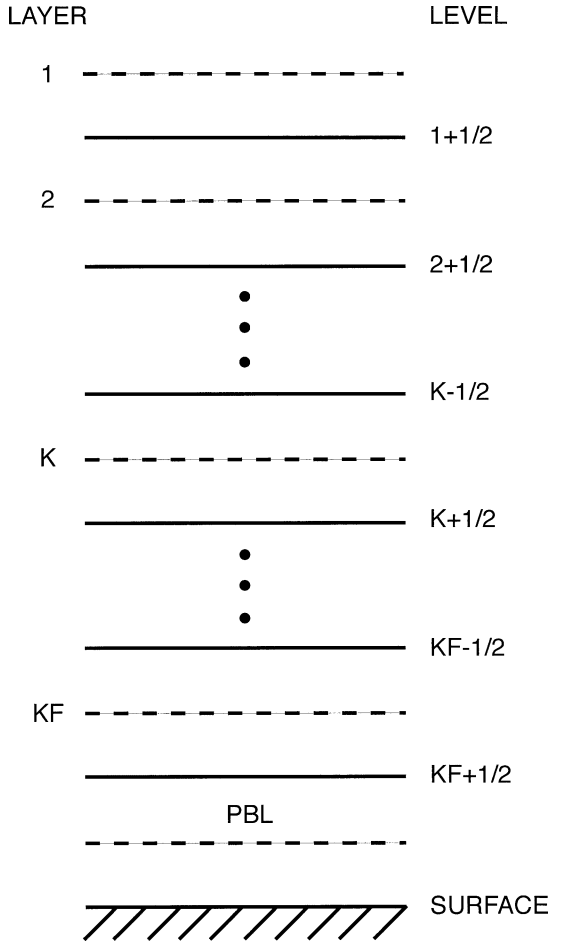

FIG. 2. Schematic of model layers, following Lord et al. (1982).

At the base of the convective updraft, we presently assume that the in-cloud thermodynamic properties are the same as those of the large-scale environment, except for rain and snow, or

$$h_c = \overline{h}; \quad q_{vc} = \overline{q}_v; \quad q_{cc} = \overline{q}_c; \quad q_{ic} = \overline{q}_i; \quad \text{and}$$
$$q_{rc} = q_{sc} = 0. \tag{14}$$

Here, we set q_{rc} and q_{sc} equal to zero because we do not parameterize the updraft vertical velocity and fall speeds of rain and snow in the convective updraft at this time. We still assume that, once formed, convective rain is instantaneously removed from the atmosphere, as in Ding and Randall (1998) and Pan and Randall (1998). Different treatments of the snow formed in the convective updraft can be considered. This is the object of the various sensitivity experiments described in the next section. Equation (14) can, of course, be easily be modified to test the sensitivity of the model results to different cloud-base conditions.

As stated above, we assume that h_c, q_{vc}, q_{cc}, and q_{ic} are lifted in the convective updraft, starting at the base of layer k. If we assume linear profiles of $\eta(\lambda)$, $h_c(k - 1/2, i)$, and $q_{xc}(k - 1/2, i)$, where x refers to the subscript v for water vapor, c for cloud water, i for cloud ice, and s for snow, Eq. (9) may be approximated by

$$h_{ck-1/2,i} = \frac{[1 + \lambda(z_{k+1/2,i} - z_B)]h_{ck+1/2,i} + \lambda\Delta z_k \overline{h}_k}{1 + \lambda(z_{k-1/2,i} - z_B)}, \tag{15}$$

and

$$q_{xck-1/2,i} = \frac{[1 + \lambda(z_{k+1/2,i} - z_B)]q_{xck+1/2,i} + \lambda\Delta z_k \overline{q}_{xk}}{1 + \lambda(z_{k-1/2,i} - z_B)} + \text{SCUP}_{xc}. \tag{16}$$

In Eqs. (15) and (16), $z_{k+1/2}$ and $z_{k-1/2}$ are the base and top heights of layer k, z_B is the cloud-base height, and Δz_k is the thickness of layer k. The first term on the right-hand sides of Eqs. (15) and (16) represents the lifting of h_c and q_{xc}, respectively, from the bottom to the top of layer k plus the entrainment of $\overline{h}$ and $\overline{q}_x$ from the sides of the updraft. Note that in both equations we assume that h_c and q_{xc} are being lifted all the way to the top of layer k, while condensation, deposition, and precipitation processes, expressed by SCUP_x in Eq. (16), are taking place. This results because we assume that microphysical and precipitation processes occur as the cloud extends upward.

We now focus on microphysical processes taking place in layer k for cloud type i, but we omit both indices to simplify the notation. First, we check whether melting (freezing) of the in-cloud ice (water) at the base of the convective updraft has taken place if the in-cloud temperature (T_c) is warmer than 0°C (colder than −20°C). As in our parameterization of large-scale cloud microphysical processes, in-cloud liquid and ice are allowed to coexist between −20°C and 0°C.

As in Lord (1978), the in-cloud saturation mixing ratio (q_{vsc}) is computed from $\overline{q}_{vs}$ by using a Taylor series approximation assuming that the difference between the in-cloud and large-scale temperatures is small, or

$$q_{vs} = \overline{q}_{vs} + \frac{\gamma}{1 + \gamma}\frac{1}{L_c}[h_c - \overline{h}_s + L_f(q_{ic} + q_{sc})], \tag{17}$$

where

$$\gamma = \left(\frac{\partial \overline{q}_{vs}}{\partial \overline{T}}\right)_p. \tag{18}$$

Here, γ is the rate of change of $\overline{q}_{vs}$ as a function of $\overline{T}$, on a constant pressure surface. It can be shown that the change in $q_{vc}(dq_{vc})$ due to condensation or deposition taking place in the convective updraft can be expressed as

$$dq_{vc} = -\frac{(q_{vc} - q_{vsc})}{1 + \gamma}. \tag{19}$$

The in-cloud temperature (T_c) is corrected accordingly, following Lord (1978):

$$T_c = \overline{T} + \frac{1}{c_p}\frac{1}{1 + \gamma}[h_c - \overline{h} + L_f(q_{ic} + q_{sc})]. \tag{20}$$

Next, we partition the amount of condensed water formed in the convective updraft (dq_{vc}) into cloud water (dq_{cc}) and cloud ice (dq_{ic}) as a function of T_c, as we did in our parameterization of large-scale cloud microphysics (Fowler et al. 1996). We assume that

$$dq_{cc} = \omega dq_{vc}, \quad \text{and} \tag{21}$$

$$dq_{ic} = (1 - \omega) dq_{vc}, \tag{22}$$

where ω is defined as

$$\omega = \frac{T_c - T_{00}}{T_0 - T_{00}}, \tag{23}$$

so that $\omega = 0$ for $T_c = T_{00}$, and $\omega = 1$ for $T_c = T_0$. In Eq. (23), T_0 is the freezing temperature ($T_0 = 0°C$) and T_{00} is the lowest threshold temperature for supercooled cloud water to form ($T_{00} = -20°C$).

Precipitation of rain follows the same method as in Ding (1995). A fraction of the cloud water formed in the convective updraft is converted to rain while the remaining fraction is lifted to the next layer. Rain can instantaneously fall to the base of the cloud, and can instantaneously fall to the surface, or be detrained into the large-scale environment. When added to the rain formed by large-scale microphysical processes, rain may evaporate as it falls through subsaturated layers at a speed that is explicitly calculated. A fraction of the cloud ice formed in the convective updraft is converted to snow, while the remaining fraction continues to be lifted to the next layer. The treatment of snow is explained in greater detail in the next section.

The amount of in-cloud water and ice converted to rain and snow is computed assuming the conversion rate

$$P = \frac{c_0 \Delta z}{(1 + c_0 \Delta z)}, \tag{24}$$

where c_0 is set to $2 \times 10^{-3}\ \mathrm{m}^{-1}$, and Δz is the thickness of the layer. Given the amount of condensed water dq_{vc} available in a layer, the rates of change in q_{cc}, q_{ic}, q_{rc}, and q_{sc} after precipitation processes have occurred are, respectively,

$$dq_{cc} = (1 - P)\omega dq_{vc}, \tag{25}$$

$$dq_{ic} = (1 - P)(1 - \omega) dq_{vc}, \tag{26}$$

$$dq_{rc} = P\omega dq_{vc}, \quad \text{and} \tag{27}$$

$$dq_{sc} = P(1 - \omega) dq_{vc}. \tag{28}$$

In the next section, we analyze the importance of including precipitation from the cold section of the convective updraft, and the treatment of convective snow on the climate simulated by the CSU GCM.

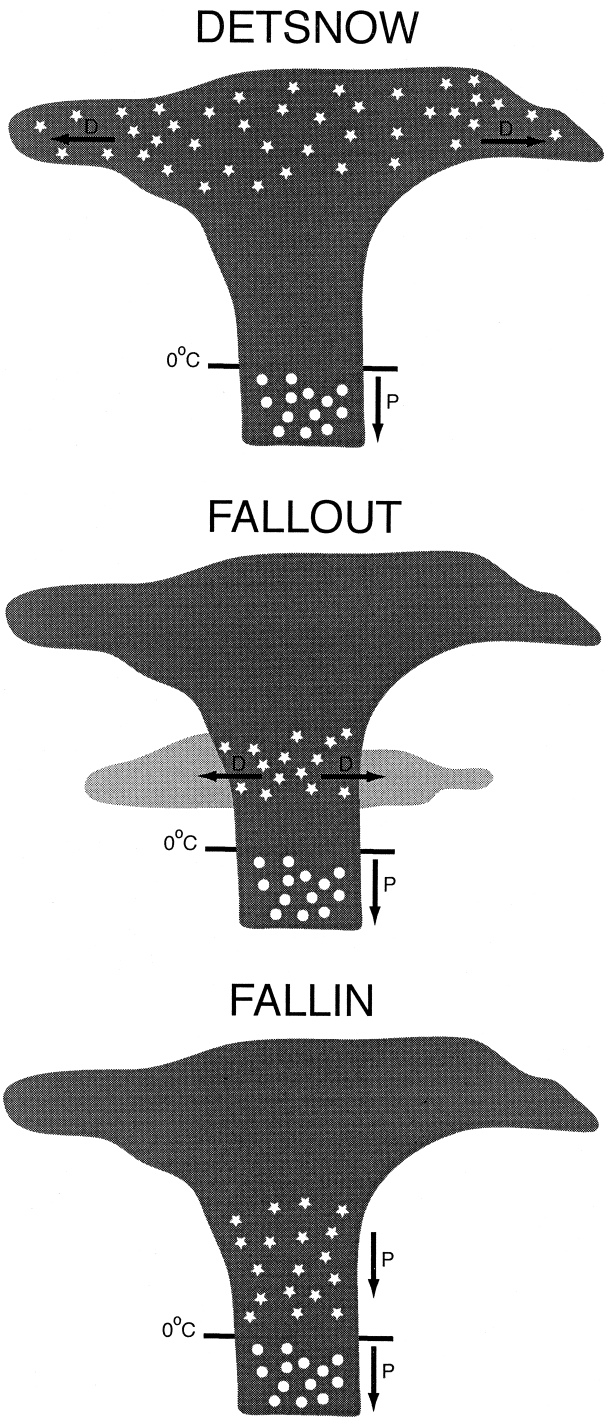

FIG. 3. Schematic of sensitivity experiments. Snow flakes are represented as stars, and rain drops are represented as dots; D indicates detrainment of snow; P refers to convective precipitation.

4. Sensitivity experiments

The preceding description of EAUCUP suggests that, while convective rain is assumed to instantaneously reach the ground, alternative assumptions can be made with regard to snow formed in the convective updrafts. We investigate the sensitivity of the hydrological cycle and atmospheric general circulation to such alternative assumptions in the three experiments described below and illustrated in Fig. 3.

- DETSNOW: In this experiment, we assume that all snow is lifted and detrained at the tops of the updrafts, as are cloud water and cloud ice. The detrained snow is then a source of snow for the parameterized large-scale cloud microphysics. Convective snow forms only through conversion of convective cloud ice, that is, 1) $q_{sc} = 0$ at the base of the updraft, and 2) large-scale snow is not entrained into the updraft, or

$$\frac{\partial}{\partial z}[\eta(z, \lambda)q_{sc}] = \mathrm{CUP}_{sc}, \tag{29}$$

  where CUP_{sc} is the convective tendency of snow due to conversion of cloud ice to snow. Because there is no loss of snow through precipitation outside or inside of the updraft, or gain of snow through entrainment from the sides of the updraft, the in-cloud generalized moist static energy is conserved during the growth of the cloud. Assuming that snow reaches cloud top without precipitating is quite extreme but not completely unreasonable since we know that the terminal velocity of snow is generally smaller than the updraft vertical velocity so that some snow will be pushed upward toward the top of the cloud.
- FALLOUT: Here, we assume that once formed, convective snow immediately falls outside of the convective updraft where it becomes a source of snow for the large-scale cloud microphysics. Under that assumption, the term $(\partial/\partial\sigma)\rho\overline{w'q_s'}$ on the right-hand side of Eq. (1) is equal to zero, and the tendency of snow due to convection is due to microphysical processes only. In contrast to DETSNOW, in which the in-cloud moist static energy is conserved, FALLOUT leads to an increase of the in-cloud moist static energy due to the loss of snow during the growth of the updraft.
- FALLIN: In this last experiment, convective snow is assumed to fall instantaneously to the base of the updraft. If the cloud-base temperature is colder than freezing, convective snow becomes a source of snow at the cloud-base level for the large-scale cloud microphysics. Below the base of the convective cloud, snow precipitates in the form of large-scale snow, which may sublimate or melt. If the cloud-base temperature is warmer than freezing, snow melts and, as convective rain, falls instantaneously to the ground. As with FALLOUT, there is no vertical transport of snow by convective circulations and the in-cloud moist static energy increases. In FALLIN, the treatment of precipitation of rain plus snow for the case of updrafts with warm cloud bases closely resembles that used by Ding and Randall (1998). As in Ding and Randall (1998), precipitation is assumed to reach the ground instantaneously, so we anticipate results similar to those obtained in their climate simulations, especially in the Tropics.

DETSNOW and FALLIN simulate extreme limits of the actual formation and precipitation of rain and snow inside convective updrafts. Assuming that snow detrains completely at cloud-tops without precipitating, or that rain falls instantaneously to the ground without evaporating is somewhat unrealistic. Nevertheless, they help explore the sensitivity of the hydrological cycle simulated by the CSU GCM under these extreme assumptions. Each experiment was run for 5 simulated years with climatological seasonally varying sea surface temperatures, starting from the same 1 November initial conditions, and results are discussed using the 5-yr January and July means. Differences among the three simulations are discussed using DETSNOW as the control simulation. The version of the CSU GCM used in this study is the same as that used by Fowler et al. (1996), except for EAUCUP.

5. Impact on convection

a. Single-column simulations

Before focusing on how the treatment of snow formed in convective updrafts modifies precipitation and the convective tendencies of the temperature and the water species between the simulations described above, we tested EAUCUP in the single-column version of the CSU GCM (SCM). As first discussed by Betts and Miller (1986), and later by Randall et al. (1996), SCMs are easy to use tools for testing parameterizations developed for use in large-scale models. The SCM was forced with the total advective tendencies prescribed from observations taken during the July 1995 intensive observation period (IOP) at the Southern Great Plains (SGP) site of the Atmospheric Radiation Measurement (ARM) project (Stokes and Schwartz 1994). The July 1995 IOP lasted for 18 days, starting at 0000 UTC 18 July 1995, and ending at 2330 UTC 4 August 1995. The *revealed forcing* method was used to prescribe the advective tendencies of temperature and water vapor, as described in Randall and Cripe (1999). Figure 4 shows time series profiles of temperature differences between (a) DETSNOW and radiosonde data taken at the ARM SGP Cloud and Radiation Testbed (CART) site, and (b) FALLIN minus DETSNOW. Figure 5 is the same as Fig. 4, but for water vapor. In DETSNOW and FALLIN, the top of the prognostic PBL depth varies between 850 and 700 hPa. Figures 4a and 5a show that the PBL is too warm and too dry relative to observations, and that upper-tropospheric temperatures are also too cold during the entire IOP. Figures 4b and 5b reveal minor differences in the simulated temperature and water vapor soundings between FALLIN and DETSNOW. In addition, a time series of the simulated and observed surface rainfall would show that FALLIN and DETSNOW successfully reproduce the first and last convective events that occurred during the IOP, but slightly underestimate the actual amount of precipitation. (This figure is not shown for brevity.) As discussed in Randall and Cripe (1999), we expect the revealed forcing to give the largest errors in the soundings. Comparing the magnitude of

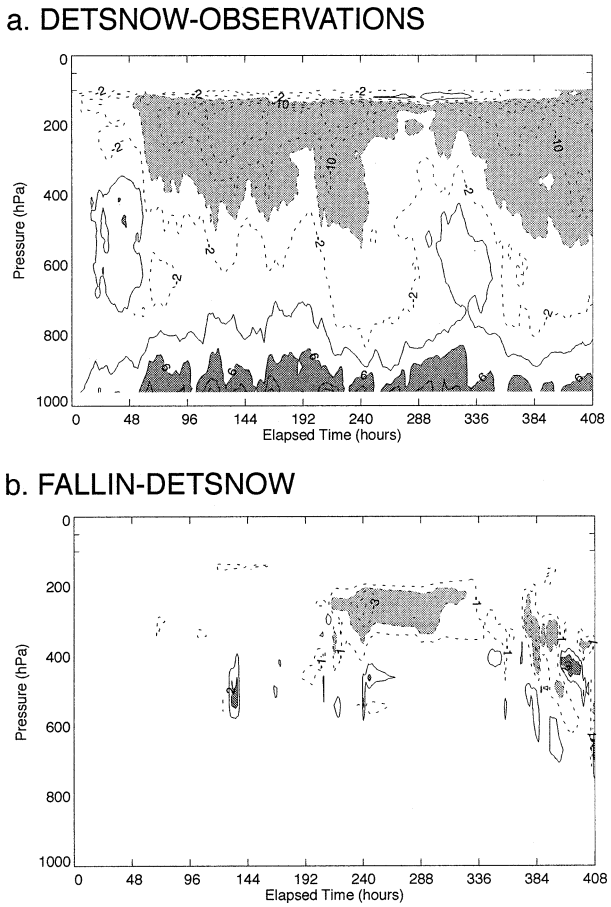

FIG. 4. Time series of the temperature difference between (a) DETSNOW and ARM data, and (b) FALLIN and DETSNOW. Units are in kelvins. In (a), light shading corresponds to differences smaller than −6 K, and dark shading corresponds to differences greater than 6 K. In (b), light shading corresponds to differences smaller than −2 K, and dark shading corresponds to differences greater than 2 K.

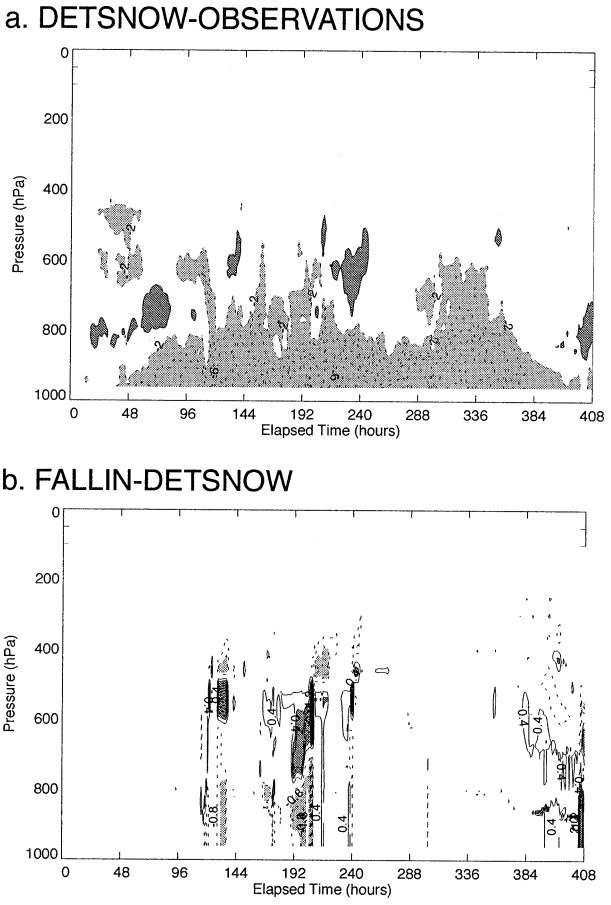

FIG. 5. Time series of the water vapor mixing ratio between (a) DETSNOW and ARM data, and (b) FALLIN and DETSNOW. Units are grams per kilogram. (a) Light shading corresponds to differences smaller than −2 g kg^{-1}, and dark shading corresponds to differences greater than 2 g kg^{-1}. (b) Light shading corresponds to differences smaller than −0.8 g kg^{-1}, and dark shading corresponds to differences greater than 0.8 g kg^{-1}.

the temperature and water vapor differences between Figs. 4a and 4b, and between Figs. 5a and 5b, shows that the atmosphere simulated by the SCM version of the GCM is not highly sensitive to the treatment of convective snow, but helps identify other model deficiencies as well. As in Randall and Cripe (1999), we used different methods to prescribe advective tendencies with DETSNOW and FALLIN. A complete description of our results is beyond the scope of this research.

b. Precipitation

Figure 6 shows the zonally averaged distributions of cumulus, large-scale, and total precipitations obtained in DETSNOW, FALLOUT, and FALLIN; Table 1 lists their respective globally averaged values. Figure 7 shows the geographical distributions of the difference in total precipitation between FALLOUT and DETSNOW, and between FALLIN and DETSNOW. Figures 8 and 9 show the geographical distributions of the simulated cumulus and large-scale precipitations in January and July. In both January and July, global means and zonally averaged profiles reveal compensating variations between the cumulus and large-scale precipitation rates so that the globally averaged total precipitation remains nearly unchanged among the three simulations. Only the tropical maximum of total precipitation simulated in FALLIN is wider than the maxima simulated in DETSNOW and FALLOUT, and only in January. The left panels of Fig. 7 show that, as expected, there are little differences in the global distribution of total precipitation between FALLOUT and DETSNOW. In contrast, Fig. 7 also reveals that the broadening of the tropical maximum between FALLIN and DETSNOW, in January, results because of the strong increase in precipitation over South America as well as along the equator over the oceans. In particular, the top left panel of Fig. 7 shows that, in the Pacific Ocean, precipitation increases and decreases north and south of the equator, respectively. In FALLIN, the increased total precipita-

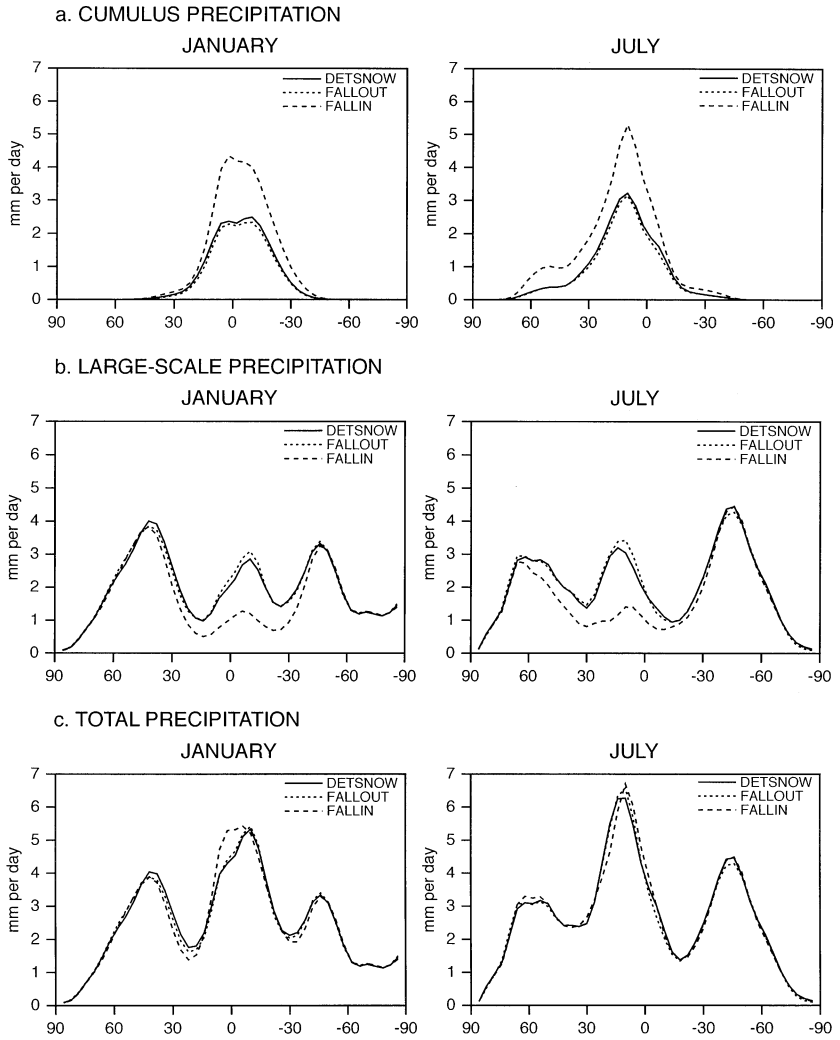

FIG. 6. Zonally averaged distributions of (a) the cumulus precipitation, (b) the large-scale precipitation, and (c) the total precipitation simulated by DETSNOW, FALLOUT, and FALLIN in Jan (left panels) and Jul (right panels). Units are millimeters per day.

tion over the Pacific Ocean results because of the increased cumulus precipitation there, as seen in Fig. 8. DETSNOW and FALLOUT yield significant decreases (increases) in cumulus (large scale) precipitation relative to FALLIN. In these two experiments, the January cumulus precipitation accounts for about 25% of the total precipitation whereas it accounts for 45% in FALLIN. In contrast, the January large-scale precipitation accounts for about 75% in both DETSNOW and FALLOUT, relative to 55% in FALLIN. Similar differences are found for July. In DETSNOW and FALLOUT, snow is removed at the top or on the sides of the updraft, and is a source of snow for EAULIQ. The only source of cumulus precipitation, which is assumed to instantaneously fall to the surface, is the conversion of cloud water to rain. Conversion rates of cloud water to rain

TABLE 1. Global means of cumulus, large-scale, total precipitations, and cumulus incidence simulated by DETSNOW, FALLOUT, and FALLIN. Units are millimeters per day for precipitation, and percent for cumulus incidence.

	Jan			Jul		
Global mean	DETSNOW	FALLOUT	FALLIN	DETSNOW	FALLOUT	FALLIN
Cumulus precipitation	0.81	0.75	1.33	0.93	0.87	1.49
Large-scale precipitation	2.15	2.17	1.62	2.22	2.25	1.66
Total precipitation	2.96	2.92	2.95	3.15	3.12	3.15
Cumulus incidence	24.3	23.8	22.3	26.8	26.4	24.7

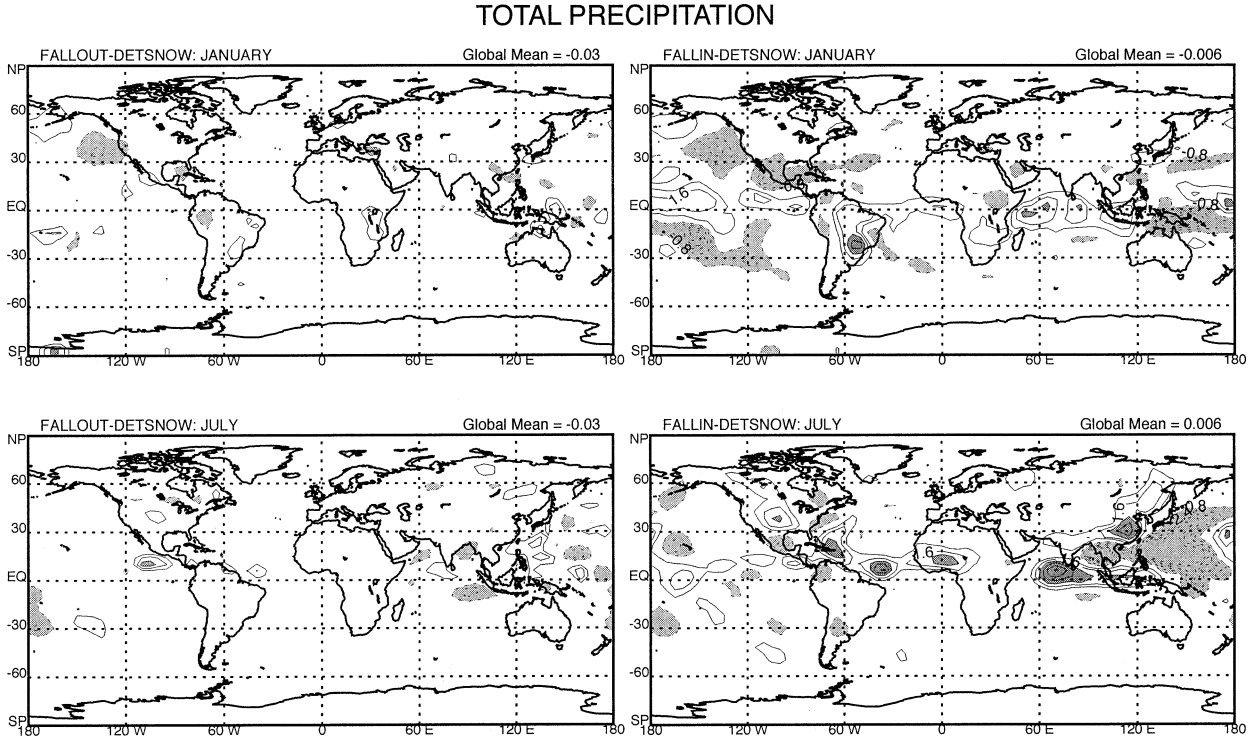

FIG. 7. Geographical distributions of the difference in total precipitation between FALLOUT and DETSNOW (left panels) and FALLIN and DETSNOW (right panels). Top and bottom panels are for Jan and Jul, respectively. Units are millimeters per day.

are small at both tropical and extratropical latitudes because, although cloud-base temperatures may be warmer than 0°C, a major fraction of the cloud sounding is colder than 0°C and ice-cloud microphysical processes dominate. Outside the updrafts, convective snow is added to the large-scale snow leading to increased large-scale precipitation or evaporation rates under super- or subsaturated conditions, respectively. In FALLIN, once formed, snow is assumed to fall instantaneously to the base of the updraft, potentially increasing the cumulus precipitation rate relative to DETSNOW and FALLOUT by melting in the first layer encountered with a temperature warmer than 0°C. The differences in the partitioning between cumulus and large-scale precipitation among DETSNOW, FALLOUT, and FALLIN are, of course, largest in the Tropics because cumulus incidence strongly decreases at higher latitudes. It is interesting to note that, on monthly timescales, the total precipitation rate is the same in the three simulations, although the partitioning between cumulus and large-scale precipitation is different, and even though cumulus precipitation falls instantaneously to the surface whereas large-scale precipitation falls with a finite speed. This result reveals a mutual adjustment between convective and large-scale moist processes so that the atmospheric moisture budget and energy budgets are essentially the same in all of DETSNOW, FALLOUT, and FALLIN.

One important issue in analyzing the hydrological cycles of DETSNOW, FALLOUT, and FALLIN is the realism of the simulated ratio between convective and large-scale precipitations. The left panels of Figs. 8 and 9 highlight the uniform increase in convective precipitation in FALLIN relative to DETSNOW and FALLOUT along the Intertropical Convergence Zone (ITCZ) over the oceans and the well-known convectively active regions over land. The right panels of Figs. 8 and 9 are more interesting because they reveal the occurrence of large-scale precipitation in conjunction with convective precipitation along the ITCZ in DETSNOW and FALLOUT, a feature that is missing in FALLIN, as seen in the eastern Pacific Ocean in July.

One objective of the Tropical Rainfall Measuring Mission (TRMM) is to provide independent global estimates of the cumulus and large-scale precipitation rates (Kummerow et al. 1998; Simpson et al. 1996). The partitioning between convective and large-scale precipitations can be obtained from brightness temperatures measured by the TRMM Microwave Imager (TMI; Anagostou and Kummerow 1997; Hong et al. 1999) or from reflectivity measurements from the TRMM precipitation radar (PR; Rosenfeld et al. 1995; Steiner and Yuter 1995). Figure 10 shows the geographical distributions of total, convective, and stratiform precipitation rates obtained from TRMM PR data (version 5) averaged between December 1999 and February 2000. On a monthly timescale, and at a spatial resolution of 5° latitude by 5° longitude, convective and stratiform precipitation each contribute about one-half of the total pre-

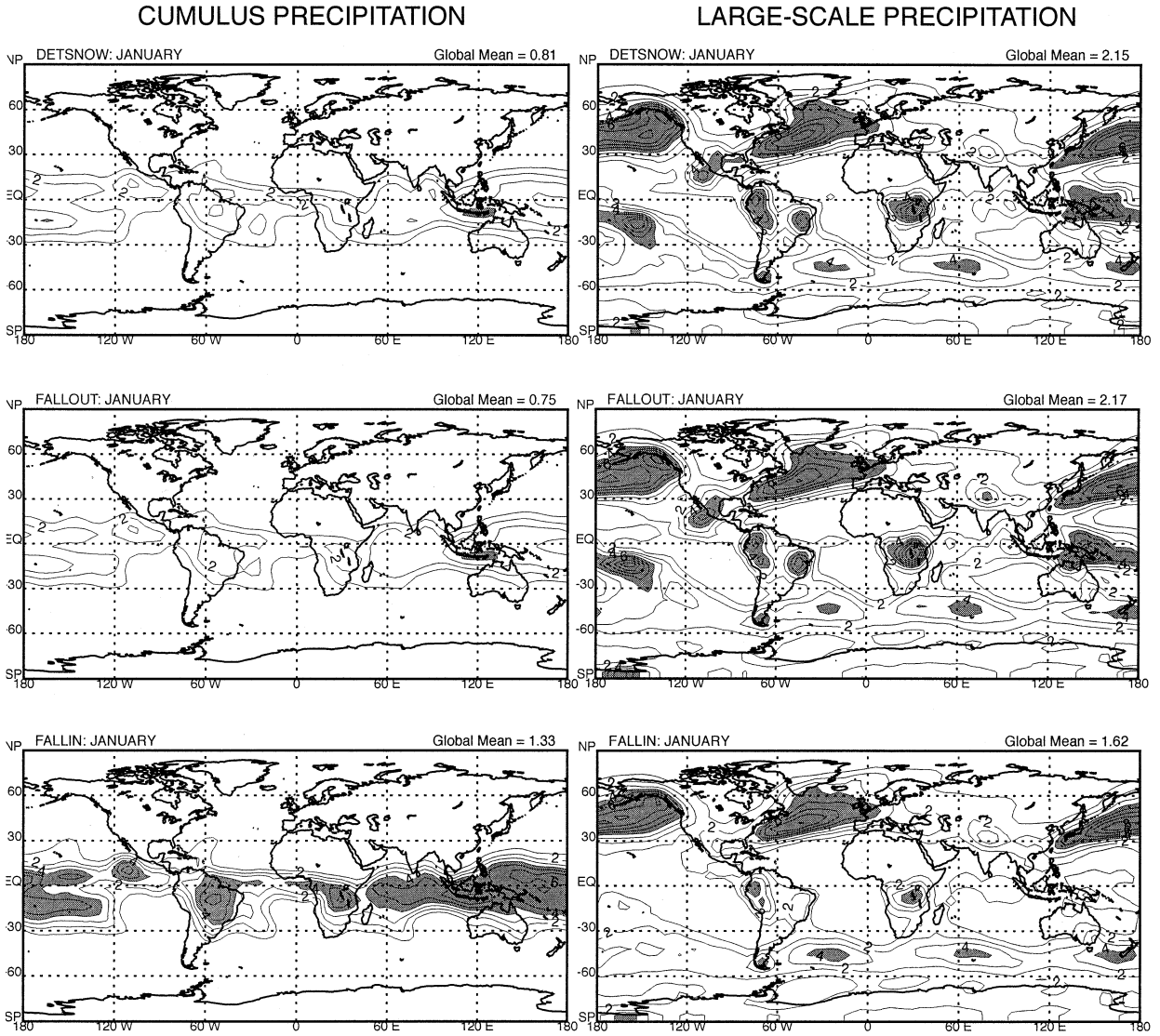

FIG. 8. Geographical distributions of the cumulus precipitation (left panels), and large-scale precipitation (right panels) simulated by DETSNOW (top panels), FALLOUT (middle panels), and FALLIN (bottom panels) in Jan. Units are millimeters per day.

cipitation (52.4% and 47.2% of the total 2.48 mm day^{-1}, respectively). Maxima of large-scale precipitation coincide with maxima of convective precipitation over land and oceans in the Tropics and higher latitudes. It is interesting to note that the convective plus stratiform precipitation rates do not exactly add up to the total rate of precipitation. The difference between the total and convective plus stratiform precipitation rates, labelled as *warm* rain is the residual of the total precipitation that cannot be classified as either convective or stratiform (Dr. J. Awaka 2000, personal communication). The amount of warm precipitation will be reduced as techniques to separate convective and stratiform precipitation are refined.

We understand that our classification of simulated convective and stratiform precipitations is not based on the same criteria as the classification used by TRMM. Nevertheless, we want to investigate if, in the CSU GCM, the partitioning between convective and stratiform precipitations resembles, at least qualitatively, that obtained in TRMM. Although we do not explicitly compute the vertical velocity of convective updrafts, our definition of convection in the CSU GCM is similar to that of Houze (1997) who uses the adjective ''convective'' to describe the precipitation (or radar echo) associated with young, active convection (maximum vertical velocity of 1–10 m s^{-1}), that is, when convective updrafts develop. Our parameterization of large-scale cloud microphysics simulates the mature stage of convection, that is, when the convective updraft is completely grown and convective anvils develop through detrainment of cloud water and cloud ice at the tops of

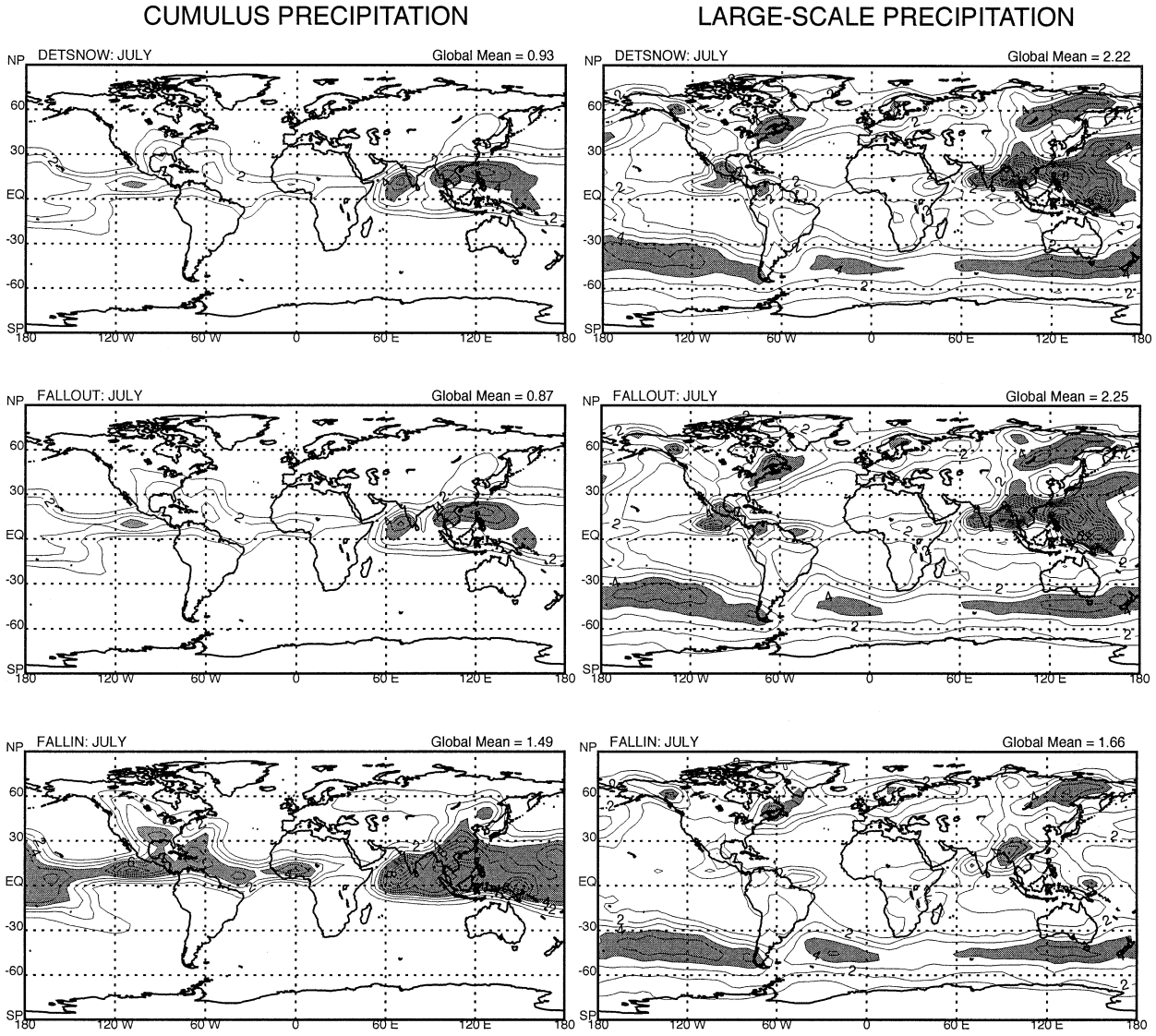

FIG. 9. As in Fig. 8, but for Jul.

the clouds. Stratiform rain and snow form and grow through the autoconversion and collection processes. The vertical velocity of stratiform rain is explicitly calculated (Fowler et al. 1996), unlike that of convective rain. At the spatial and temporal resolutions of the CSU GCM, our simulation of horizontally spreading anvils is similar to the definition of stratiform precipitation of Houze (1997) who uses the adjective ''stratiform'' to refer to precipitation occurring in older, less active convection and possessing radar echoes that have weak horizontal gradients and/or bright bands (maximum vertical velocity of 1–2 m s^{-1}). Therefore, it is reasonable to compare, at least in a broad manner, the simulated and satellite-derived convective and large-scale precipitation rates. As seen in Fig. 10, satellite-derived convective and large-scale precipitation rates from TRMM PR data display similar geographical distributions suggesting that, in the Tropics, large-scale precipitation is primarily produced by decaying convective systems. In the CSU GCM, intense large-scale precipitation is also found far from convectively active areas, as seen over the Andes in January. Over mountain ranges, large-scale precipitation forms through autoconversion and collection processes in layers in which the large-scale relative humidity exceeds 100%.

c. Convective tendencies

Each tendency includes a contribution due to microphysical processes occurring during the growth of the updraft [as described by the first term on the rhs of Eqs. (1) and (2)], plus a contribution due to vertical transport by convective circulations [as described by the second term on the rhs of Eqs. (1) and (2)]. As an example,

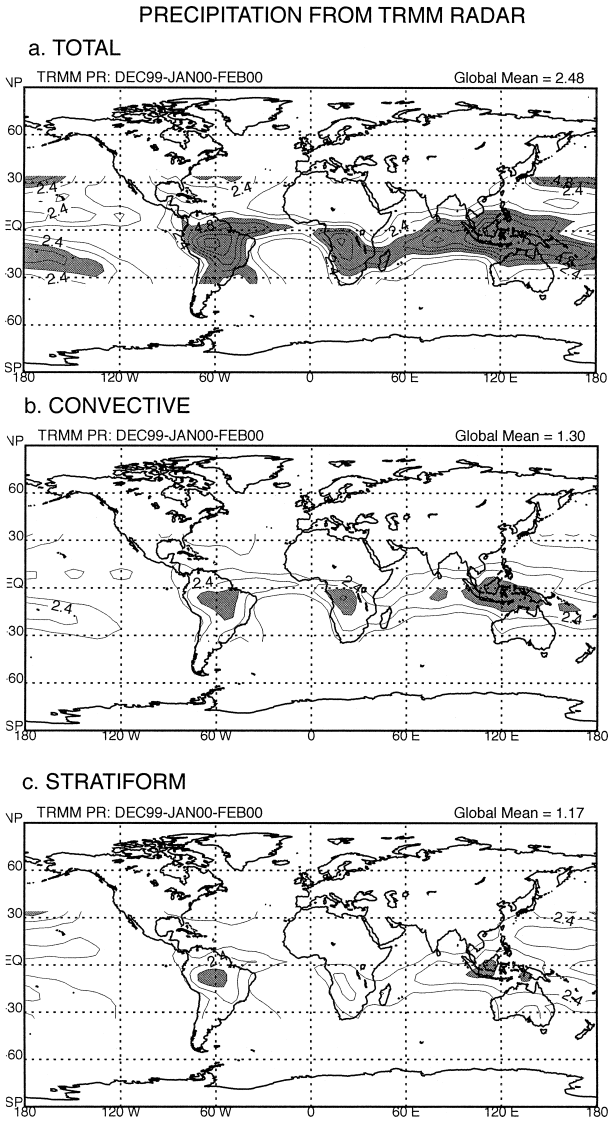

FIG. 10. Geographical distributions of (a) the total precipitation, (b) the convective precipitation, and (c) stratiform precipitation obtained from TRMM PR data, for Dec–Jan–Feb. Units are millimeters per day.

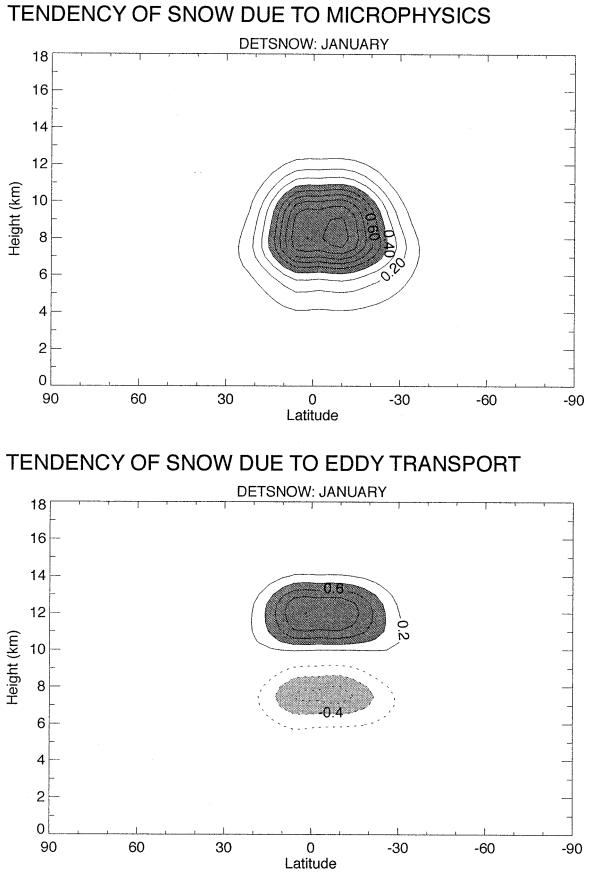

FIG. 11. Latitude–height cross sections of (a) the zonally averaged convective tendency of snow due to cloud microphysical processes occuring in the updraft, and (b) the zonally averaged tendency of snow due to transport by cumulus circulations simulated by DETSNOW. Units are grams per kilograms per day.

Fig. 11 shows the contributions of the tendencies of snow due to microphysics and cumulus transport to the total tendency of snow in DETSNOW. As explained earlier, convective snow is detrained at the tops of the updrafts and acts as a source of large-scale snow, simulating the growth of extended icy anvils at the tops of narrow cumulus towers. The effect of the vertical transport by cumulus circulations is to raise the level at which maximum detrainment occurs by moving snow from lower to higher levels in the updrafts, causing snow to be detrained at about 12 km, rather than at 9 km, which is the level where the generation of snow due to microphysical processes has a maximum.

The latitude–height cross sections of the zonal-mean convective tendency of temperature (i.e., the convective heating rate) in DETSNOW, and the differences between the zonal-mean convective heating rates in FALLOUT and DETSNOW, and FALLIN and DETSNOW, are shown in Fig. 12. There is more convective heating in DETSNOW. We now discuss the reasons for this. The difference $c_p(dT_{\mathrm{FALL}} - dT_{\mathrm{DET}})$ between the temperature tendencies simulated in FALLOUT and DETSNOW (or FALLIN and DETSNOW) can be written as

$$c_p(dT_{\mathrm{FALL}} - dT_{\mathrm{DET}}) = (dh_{\mathrm{FALL}} - dh_{\mathrm{DET}}) - L_v(dq_{v\mathrm{FALL}} - dq_{v\mathrm{DET}}) + L_f(dq_{is\mathrm{FALL}} - dq_{is\mathrm{DET}}). \quad (30)$$

The three terms on the rhs of Eq. (30) are differences between the convective tendencies of moist static energy, water vapor, and cloud ice plus snow, respectively. By successively analyzing the changes in each term on the rhs of Eq. (30), we can understand why removing convective snow on the sides or at the bottom of the updrafts leads to decreased convective heating in both FALLOUT and FALLIN, relative to DETSNOW. Figure 13 is similar to Fig. 12, but for the zonal-mean tenden-

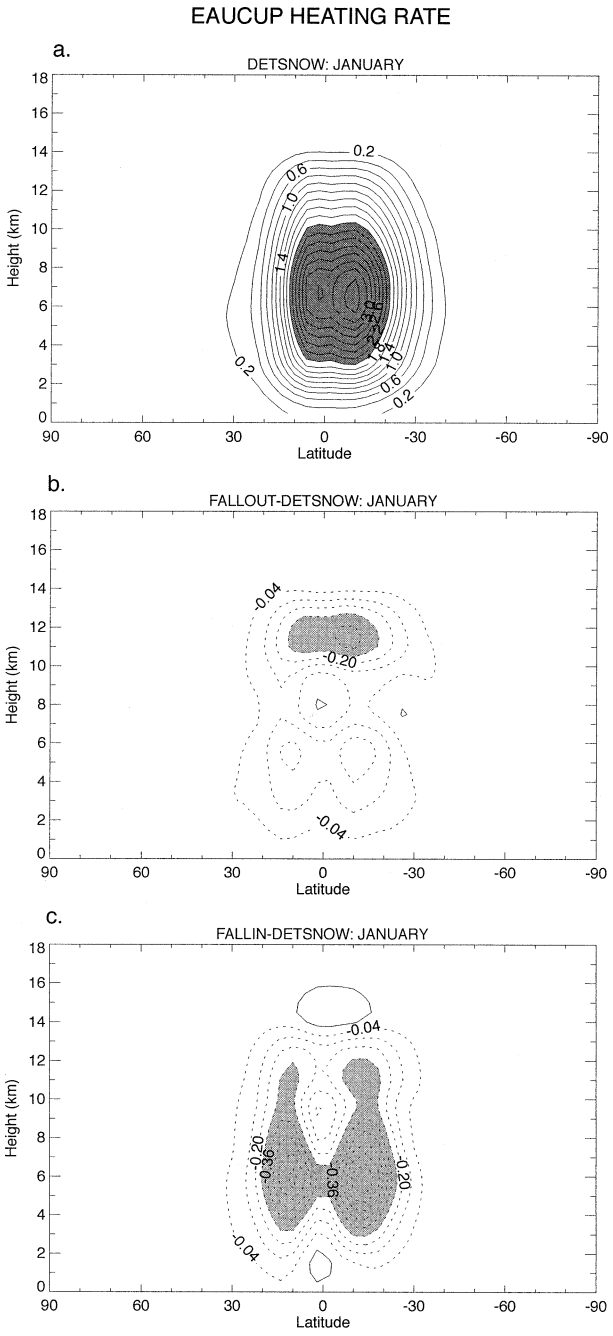

FIG. 12. Latitude–height cross sections of (a) the zonally averaged convective heating rate simulated by DETSNOW, and the difference in the zonally averaged convective heating rate between (b) FALLOUT and DETSNOW, and (c) FALLIN and DETSNOW. Units are Kelvins per day.

cies of moist static energy (Fig. 13a), water vapor (Fig. 13b), and cloud ice plus snow (Fig. 13c), respectively. In Fig. 13, all the convective tendencies are expressed in Kelvins per day for easier comparison against the convective heating rate, also expressed in Kelvins per day in Fig. 12. Figure 13a shows an increased tendency of moist static energy in FALLOUT and FALLIN, relative to DETSNOW. In DETSNOW, moist static energy is conserved in the absence of entrainment during the growth of the updraft, whereas it increases in FALLOUT and FALLIN due to the loss of snow on the sides or at the bottom of the cloud. In DETSNOW, the tendency of moist static energy due to cloud microphysical processes is zero and the total tendency is, therefore, equal to that due to vertical transport by convective circulations. Figure 13a shows decreased (increased) moist static energy at lower (upper) tropospheric levels. The difference ($dh_{\mathrm{TOT}} = dh_{\mathrm{FALL}} - dh_{\mathrm{DET}}$) between the tendencies of moist static energy simulated in DETSNOW and FALLOUT (or FALLIN) can be expanded as

$$dh_{\mathrm{TOT}} = (dh_{\mathrm{FALL}} - dh_{\mathrm{DET}})_{\mathrm{MICRO}} + (dh_{\mathrm{FALL}} - dh_{\mathrm{DET}})_{\mathrm{TRANS}}, \quad (31)$$

where the first and second terms on the rhs of Eq. (31) are differences in the tendencies of moist static energy due to microphysical processes and vertical transport by convective circulations, respectively. In Eq. (31), dh_{TOT} mainly depends on $(dh_{\mathrm{FALL}})_{\mathrm{MICRO}}$ because $(dh_{\mathrm{DET}})_{\mathrm{MICRO}}$ is equal to zero and $(dh_{\mathrm{FALL}} - dh_{\mathrm{DET}})_{\mathrm{TRANS}}$ is small relative to $(dh_{\mathrm{FALL}} - dh_{\mathrm{DET}})_{\mathrm{MICRO}}$ because dh_{FALL} and dh_{DET}, due to convective transport, almost cancel each other. Finally, dh_{FALL} and dh_{TOT} are positive because a loss of convective snow yields an increased moist static energy inside the updraft, as seen in Figs. 13b and 13c. In Fig. 13c, the decrease in dh_{TOT} on the northern flank of its maximum may be associated with the broadening of the maximum in total precipitation, as seen in Fig. 6c.

On monthly timescales, differences in convective tendencies between the three experiments result not only because of differences between the convective cloud models, but also because of differences in the response of the hydrological cycle, especially that of large-scale cloud microphysical processes. Figure 13b shows that removing convective snow on the sides or at the bottom of updrafts yields decreased convective drying of water vapor relative to the drying obtained in DETSNOW. This is not due to a reduction in convective activity. Table 1 shows that the globally averaged cumulus incidence in FALLOUT is about equal to that in DETSNOW, whereas it is slightly reduced in FALLIN relative to DETSNOW, in both January and July. Maps of the cumulus incidence would also show little variation in the geographical distributions of convection between the three simulations, indicating that the decreased tendency of water vapor results because the troposphere becomes drier in FALLOUT and FALLIN relative to DETSNOW, and not because of reduced convective activity. This point will be discussed at greater length in section 6.

Figure 13c displays a strong decrease in the tendency of snow at upper-tropospheric levels in FALLOUT and FALLIN relative to DETSNOW, which is to be expected since the tendency of snow due to vertical transport by convective circulations is equal to zero in both exper-

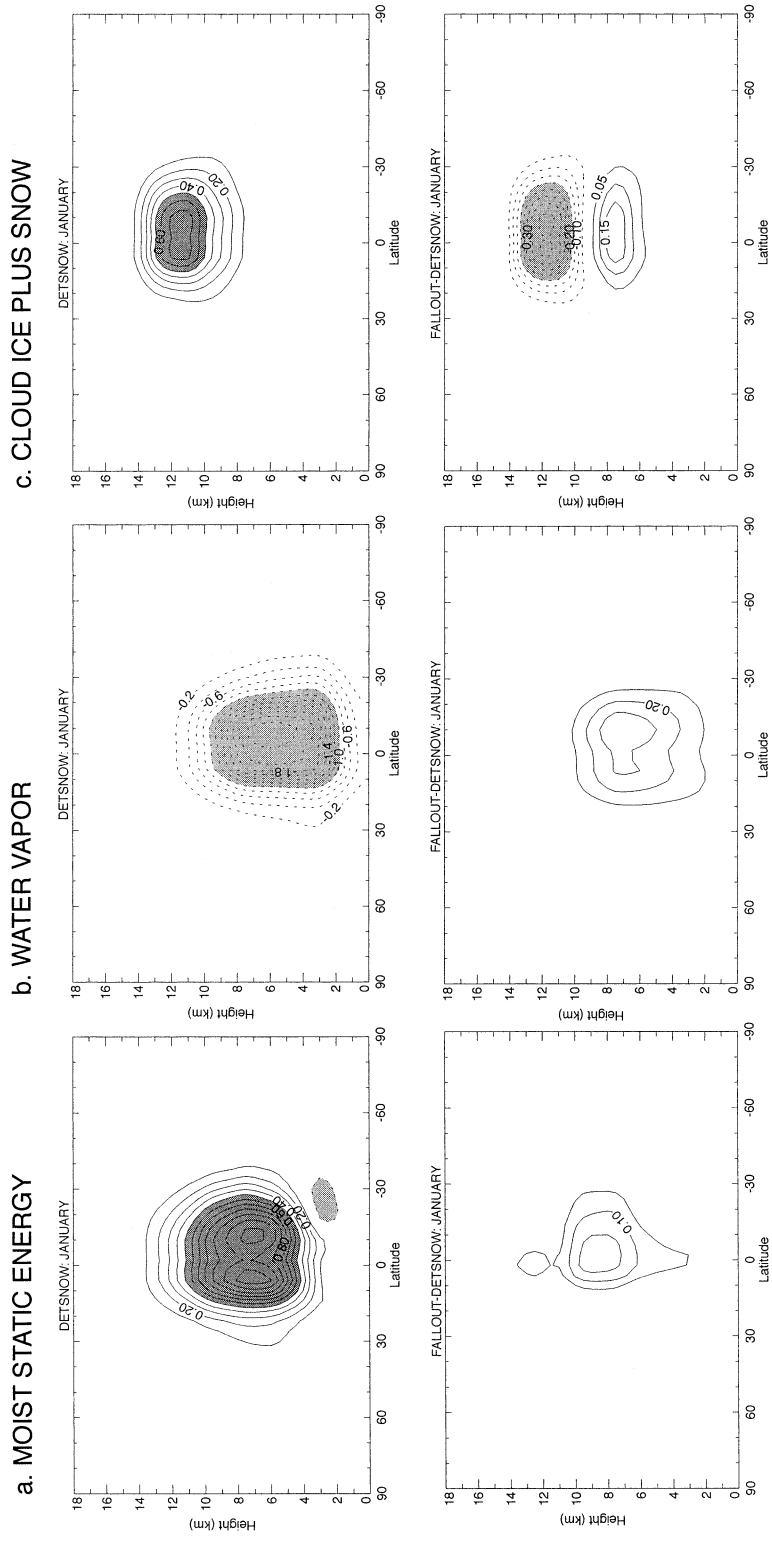

FIG. 13. Latitude–height cross sections of the zonally averaged convective tendencies simulated by DETSNOW (top panels), and the differences in the zonally averaged convective tendencies between FALLOUT and DETSNOW (middle panels), and FALLIN and DETSNOW (bottom panels): (a) moist static energy, (b) water vapor, and (c) cloud ice plus snow. Units are kelvins per day.

iments. In FALLOUT and FALLIN, the total tendency of snow being equal to that due to microphysical processes only, convective snow acts as a source of snow for the large-scale cloud microphysics at lower levels than in DETSNOW, as seen in the middle and bottom panels of Fig. 13c. Looking at Eq. (30), the decreased tendency of snow in FALLOUT and FALLIN, relative to DETSNOW leads to decreased convective heating rates.

Looking back at Fig. 12, we can now conclude that the decrease in convective heating in FALLOUT and FALLIN relative to DETSNOW occurs in conjunction with the decreased convective drying in the lower troposphere (below 8 km), and the decreased source of cloud ice plus snow in the upper-troposphere (above 10 km). Comparing Fig. 13b against 13c shows that, in FALLOUT relative to DETSNOW, the change in the convective tendency of cloud ice plus snow in the upper troposphere is greater than the change in the convective drying in the lower troposphere, so that the change in the convective heating between FALLOUT and DETSNOW is the largest in the upper troposphere (refer to Fig. 12b). Comparing FALLIN to DETSNOW shows that the change in the convective drying is greater than the change in the convective source of cloud ice plus snow, so that the change in the convective heating is greater in the lower than the upper troposphere (refer to Fig. 12c).

In general, absolute differences in the zonal mean tendencies between FALLIN and DETSNOW are greater than between FALLOUT and DETSNOW. This is particularly true of differences between convective heating and moistening of the lower troposphere. This result makes sense since, in both DETSNOW and FALLOUT, the only way convective snow contributes to precipitation is by acting as a source of snow for large-scale cloud microphysical processes, while in FALLIN convective snow directly contributes to convective precipitation through melting to become convective rain. In DETSNOW and FALLOUT, the fraction of large-scale snow detrained at the tops or on the sides of the updrafts can significantly modify the large-scale environment by enhancing evaporative cooling in subsaturated layers, and by collecting cloud water and cloud ice as it falls. This added complexity does not exist in FALLIN, especially in the Tropics where convective snow is instantaneously removed from the atmosphere in the form of convective rain.

6. Impact on large-scale processes

As explained in section 3, there exists a two-way interaction between EAUCUP and EAULIQ processes. EAUCUP interacts with EAULIQ by letting cloud water, cloud ice, and snow formed in convective updrafts act as sources of large-scale cloud water, cloud ice, and snow, thus favoring the growth of anvils. In turn, EAULIQ enhances EAUCUP microphysical processes by letting large-scale cloud water and cloud ice be lifted inside the convective updrafts. The interaction from the convective to the large-scale environment dominates over that from the large-scale to the convective environment, especially through the radiative effects of optically thick anvils. Nevertheless, the effects of the large-scale clouds on the convective clouds are important.

Latitude–height cross sections of the zonally averaged large-scale tendencies of temperature (i.e., large-scale heating rate), water vapor (i.e., large-scale moistening rate defined as positive), and cloud ice plus snow simulated in DETSNOW are shown on the top panels of Figs. 14a, 14b, and 14c, respectively. Differences in these zonally averaged large-scale tendencies between FALLOUT and DETSNOW (middle panels) and between FALLIN and DETSNOW (bottom panels) are also plotted.

As seen in the top panels of Figs. 14a and 14b, the EAULIQ response to the EAUCUP convective drying and heating of the tropical troposphere below 10 km is large-scale moistening and cooling with maxima occurring at about 6 km in DETSNOW. In the tropical upper troposphere, the EAULIQ response to the EAUCUP convective moistening, mostly through water vapor transport by convection, and production of supersaturated conditions, is large-scale condensation and warming, with maxima at about 12 km. Large-scale condensation and heating are, of course, also very active in the middle latitudes, especially in the winter hemisphere.

As seen in the middle and bottom panels of Figs. 14a and 14b, the reduced convective heating and drying of the tropical troposphere between FALLOUT and DETSNOW, and between FALLIN and DETSNOW, are associated with decreased large-scale cooling and moistening below 10 km. This makes sense because the intensity of cooling due to large-scale evaporation/sublimation is driven by the intensity of convective condensation/deposition warming. As shown in Fig. 13c, FALLOUT and FALLIN yield decreased convective sources of large-scale cloud ice and snow, relative to DETSNOW. Accordingly, we found decreased EAULIQ tendencies of cloud ice plus snow in FALLOUT and FALLIN since, in the Tropics, convective detrainment is the major source of formation of large-scale cloud ice and snow. Decreased large-scale moistening also leads to reduced deposition of water vapor on cloud ice, and reduced autoconversion of cloud ice to snow between FALLOUT and DETSNOW, and between FALLIN and DETSNOW.

7. Impact on the atmospheric general circulation

Finally, we discuss the impact of EAUCUP on the atmospheric general circulation. Modifying EAUCUP and EAULIQ tendencies of cloud ice and snow directly influences the vertical distributions of long- and shortwave radiative heating rates through changes in the up-

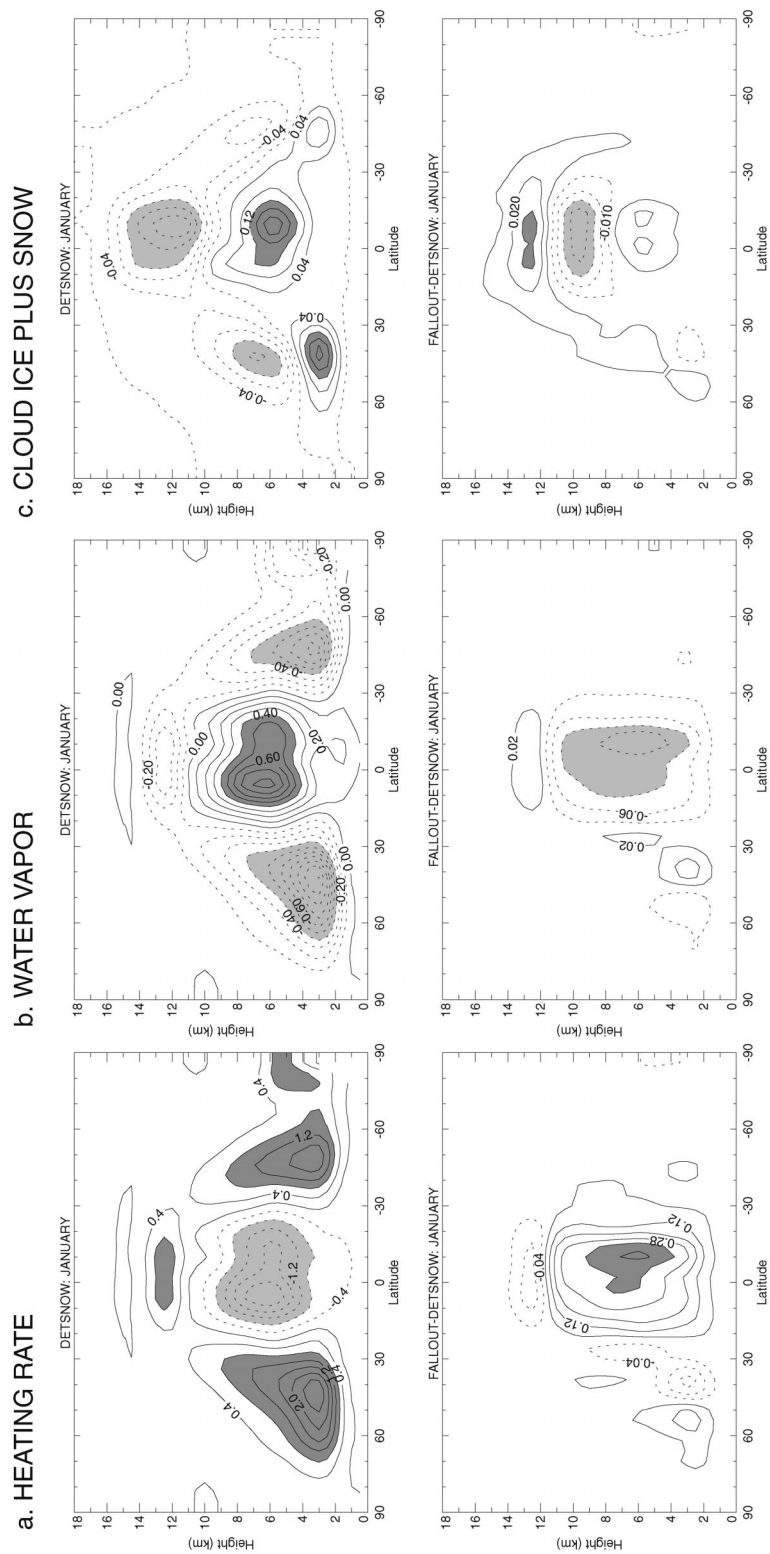

FIG. 14. Latitude–height cross sections of the zonally averaged large-scale tendencies simulated by DETSNOW (top panels), and the differences in the zonally averaged large-scale tendencies between FALLOUT and DETSNOW (middle panels), and FALLIN and DETSNOW (bottom panels): (a) heating rate in kelvins per day, (b) water vapor in grams per kilograms per day, and (c) cloud ice plus snow in grams per kilograms per day.

TABLE 2. Global means of vertically integrated cloud fraction (%), TOA outgoing longwave radiation, and planetary albedo (%).

	Jan			Jul		
Global mean	DETSNOW	FALLOLUT	FALLIN	DETSNOW	FALLOUT	FALLIN
Cloud fraction	83.3	81.5	78.4	78.6	76.5	73.6
Outgoing longwave radiation	207.2	209.3	214.0	216.0	218.3	222.5
Planetary albedo	35.9	34.9	32.8	34.9	34.6	32.8

per-tropospheric cloudiness between the three climate experiments.

One weakness of the CSU GCM is its lack of a parameterization of fractional cloudiness, although work is underway to include a prognostic equation for the cloud fraction (Randall and Fowler 1999; Fowler and Randall 2000). Except in the PBL, where the formulation of cloudiness and its optical properties follows Harshvardhan et al. (1989), clouds are assumed to form when and where the total amount of condensate exceeds 10^{-5} kg kg^{-1} and their horizontal cloud fraction is equal to 1, as discussed at length by Fowler et al. (1996). Here, we define the total amount of condensate as the amount of cloud water plus cloud ice plus snow present in a $4° \times 5°$ grid box, but limit the long- and shortwave radiative effects of snow by fixing the effective radius of snow at 1000 μm, as discussed by Fowler and Randall (1996).

In DETSNOW, the detrainment of snow at the tops of updrafts yields a significant increase in the coverage of tropical anvils, which in turn leads to a decreased top-of-the-atmosphere (TOA) outgoing longwave radiation and an increased planetary albedo, relative to FALLOUT and FALLIN, as seen in Table 2. Differences in the globally averaged cloud fraction, TOA outgoing longwave radiation, and planetary albedo are, as expected, the largest between FALLIN and DETSNOW. In the three simulations, we did not attempt to tune the model so that the outgoing longwave radiation, planetary albedo, and cloudiness match those obtained with the ''operational'' parameterization of convection based on Ding and Randall (1998), and Pan and Randall (1998). The reason is that, in this study, we are mainly interested in the effects of the alternative treatments of convective snow while keeping all the other parameterizations untouched.

Figure 15 shows latitude–height cross sections of the longwave, shortwave, and total cloud radiative forcings simulated by DETSNOW (top panels), and the difference in the long- and shortwave cloud radiative forcings between FALLOUT and DETSNOW (middle panels) and FALLIN and DETSNOW (bottom panels). We define the longwave cloud radiative forcing (LW_{crf}) as the difference between the clear-sky and all-sky longwave radiative cooling rates (at long wavelengths, cooling is defined as positive). In the Tropics, LW_{crf} is positive (indicating warming) below the cloud bases and negative (indicating cooling) above the cloud tops of upper-tropospheric clouds. We define the shortwave cloud radiative forcing (SW_{crf}) as the difference between the all-sky and clear-sky shortwave radiative heating rates (at short wavelengths, heating is defined as positive). SW_{crf} is negative (indicating cooling) below cloud bases and positive (indicating warming) above cloud tops. Because the magnitude of SW_{crf} is less than that of LW_{crf}, the net radiative forcing of tropical anvils is positive (warming) below cloud bases and negative (cooling) above cloud tops.

At long and short wavelengths, decreased upper-tropospheric tropical anvils in FALLOUT and FALLIN relative to DETSNOW yield decreased LW_{crf} and SW_{crf}. Because LW_{crf} is greater than SW_{crf}, the change in the net cloud radiative forcing between FALLOUT and DETSNOW, and FALLIN and DETSNOW is similar to that of LW_{crf}: the decrease in upper-tropospheric cloudiness in FALLOUT and FALLIN relative to DETSNOW yields a decreased net radiative cooling above cloud top and a decreased net radiative warming below cloud base.

We define the diabatic heating rate (Fig. 16c) as the sum of the latent heating rate (Fig. 16a), plus the heating rate due to dry convective adjustment (not shown), and the net radiative heating rate (Fig. 16b). We define the latent heating rate as the sum of the convective (EAUCUP) and large-scale (EAULIQ) heating rates (refer to Figs. 12a and 14a, respectively). In Figs. 16a and 16c, the latent and diabatic heating rates do not include any heating due to PBL processes. The middle and bottom panels of Fig. 16a show an increase in latent heating below 10 km and a decrease in latent heating above in FALLOUT and FALLIN relative to DETSNOW in the Tropics. Looking back at Figs. 12b and 12c for EAUCUP, and the middle and bottom panels of Fig. 14a for EAULIQ reveals that the increased latent heating between FALLOUT and FALLIN relative to DETSNOW below 10 km results primarily because of the increased large-scale condensation heating when snow is removed on the sides or at the bottoms of the convective updrafts. Above 10 km, the decreased latent heating results primarily because of the decreased convective heating in the upper-troposphere. The effect of tropical upper-tropospheric clouds on the vertical profiles of net radiative heating rates (where positive and negative net heating rates indicate warming and cooling, respectively) is to decrease (increase) the net radiative heating of the atmosphere above (below) the clouds. The decrease in tropical anvils between FALLOUT and DETSNOW, and between FALLIN and DETSNOW, yields an increased (decreased) net radiative heating above (below) the an-

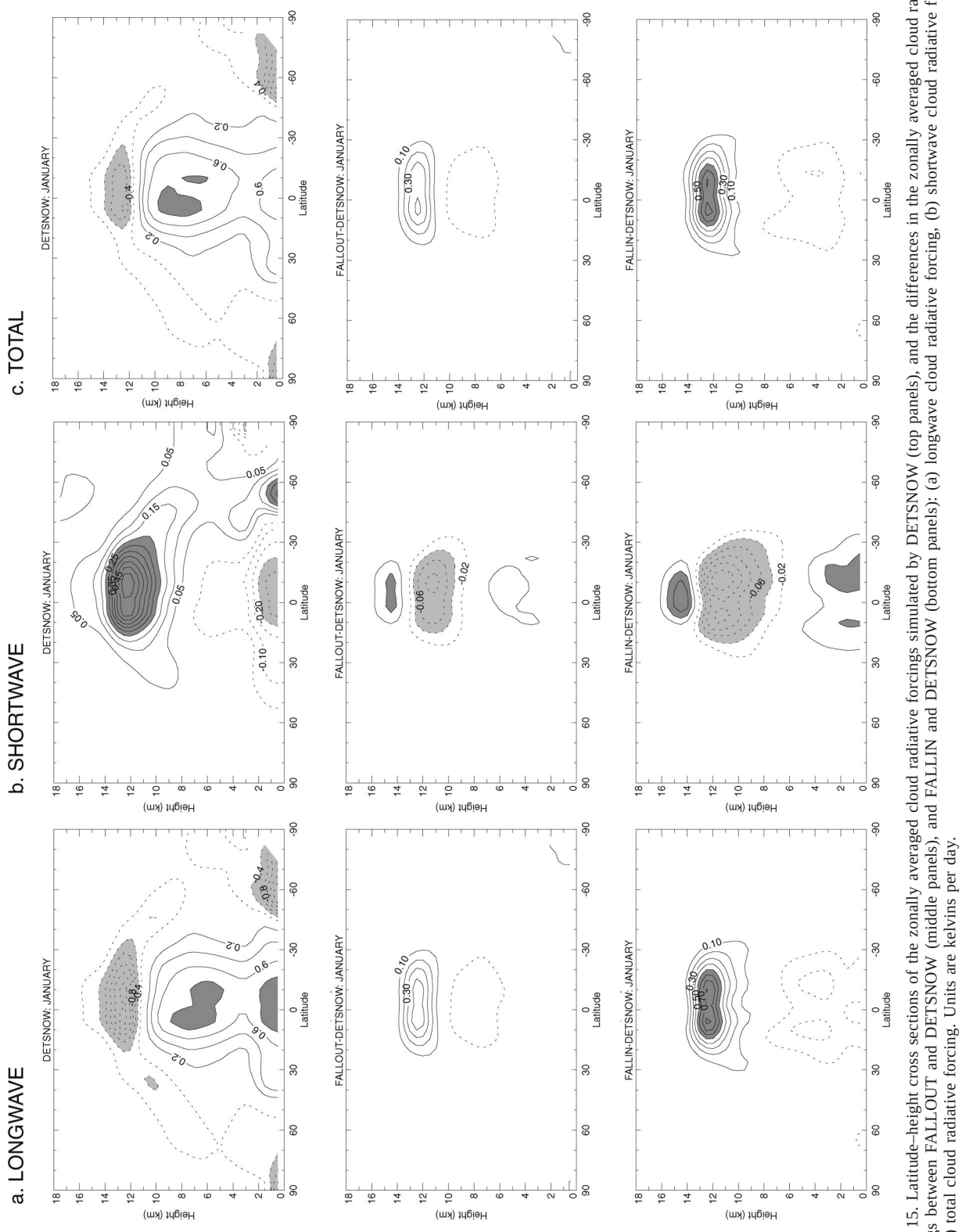

FIG. 15. Latitude–height cross sections of the zonally averaged cloud radiative forcings simulated by DETSNOW (top panels), and the differences in the zonally averaged cloud radiative forcings between FALLOUT and DETSNOW (middle panels), and FALLIN and DETSNOW (bottom panels): (a) longwave cloud radiative forcing, (b) shortwave cloud radiative forcing, and (c) total cloud radiative forcing. Units are kelvins per day.

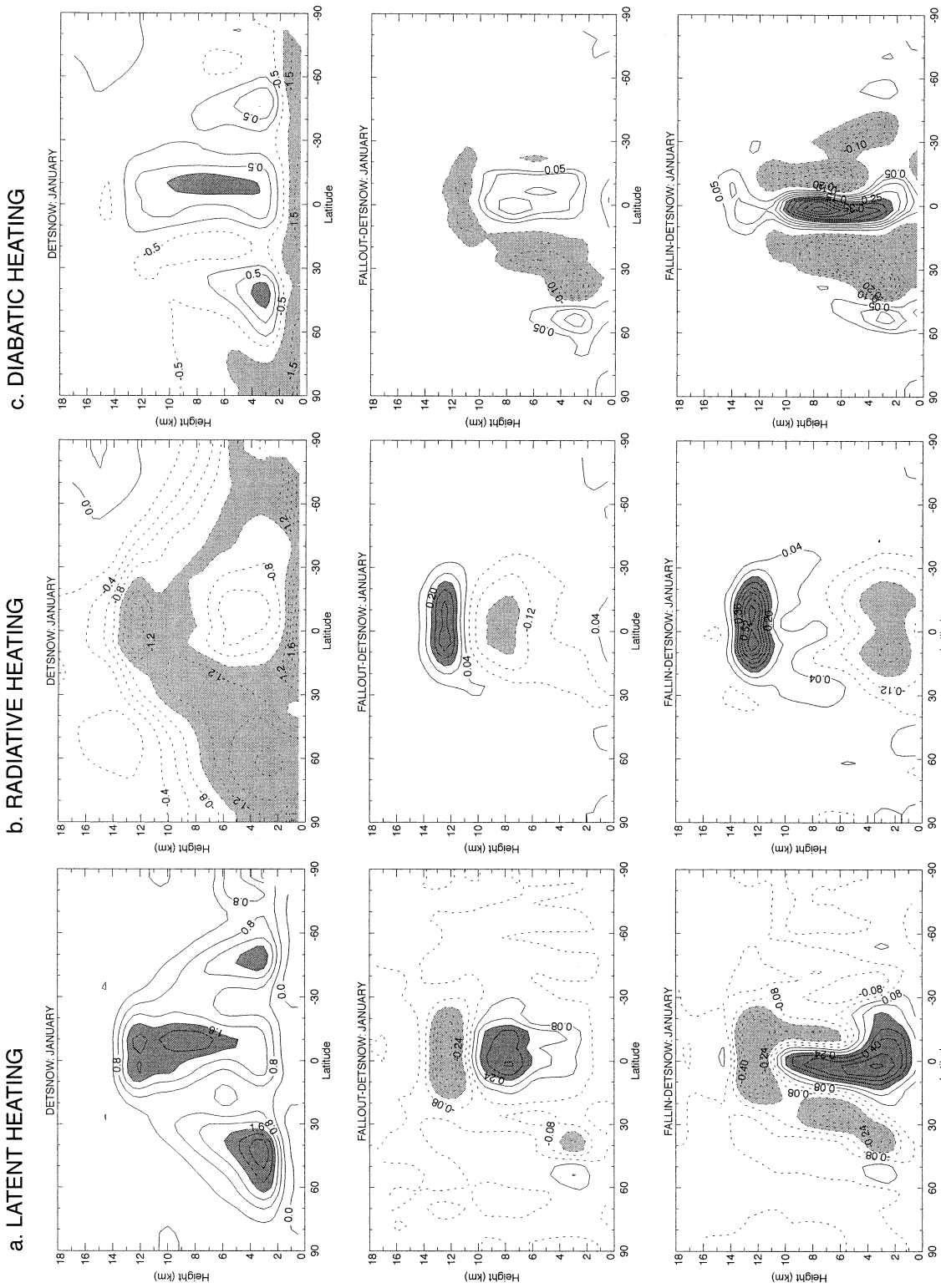

FIG. 16. Latitude–height cross sections of the zonally averaged heating rates simulated by DETSNOW (top panels), and the differences in the zonally averaged heating rates between FALLOUT and DETSNOW (middle panels), and FALLIN and DETSNOW (bottom panels): (a) latent heating rate, (b) radiative heating rate, and (c) diabatic heating rate. Units are kelvins per day.

vils, which is to be expected. As shown in 16c, the difference in diabatic heating between FALLOUT and DETSNOW, and between FALLIN and DETSNOW, varies with height, depending on the contribution in the change in latent and net radiative heatings to that in the diabatic heating between the three simulations. The middle panel of Fig. 16c shows that the greatest change in diabatic heating between FALLOUT and DETSNOW is a decrease in diabatic heating in the upper troposphere that results because of decreased latent heating, as seen in the middle panel of Fig. 16a. The bottom panel of Fig. 16c reveals an increase in the zonally averaged diabatic heating through the whole tropical troposphere in FALLIN relative to DETSNOW. This increased diabatic heating results because of increased latent heating of the troposphere below the tropical anvils, and increased net radiative heating above the tropical anvils between FALLIN and DETSNOW. Diabatic heating is reduced in the extratropics in both FALLOUT and FALLIN, relative to DETSNOW.

Finally, latitude–height cross sections of the zonally averaged relative humidity, temperature, and zonal-mean wind simulated by DETSNOW (top panels), and their differences between FALLOUT and DETSNOW (middle panels), and FALLIN and DETSNOW (bottom panels), are shown in Figs. 17a, 17b, and 17c, respectively. Figure 18 shows latitude–height cross sections of the differences between the zonally averaged profiles of temperature and zonal wind simulated by DETSNOW, FALLIN, and reanalysis data from the European Centre from Medium-Range Weather Forecasts (ECMWF). Through radiative–convective interactions, detrainment of snow at the tops of convective updrafts by EAUCUP produces a simulated climate that is wetter but colder in the Tropics than when convective snow is removed on the sides or at the bottoms of the updrafts. Differences in the zonal-mean relative humidity and temperature are, of course, larger between FALLIN and DETSNOW, than between FALLOUT and DETSNOW. As seen in Fig. 18, the cooling seen in DETSNOW relative to FALLOUT and FALLIN helps reduce the warm bias of the tropical troposphere when compared against ECMWF data. Comparisons between the precipitable water simulated by FALLIN relative to that retrieved by the National Aeronautics and Space Administration (NASA) Water Vapor Atmospheric Project (NVAP; Randel et al. 1996) show that the climate simulated with the CSU GCM is too wet relative to observations. Increasing the relative humidity, and hence the water vapor mixing ratio, in both FALLOUT and DETSNOW relative to FALLIN, leads the simulated climate further away from the observed climate. Differences in the globally averaged precipitable water relative to NVAP data increase from 4.1 kg m^{-2} in FALLIN to 5.6 kg m^{-2} in FALLOUT and 5.4 kg m^{-2} in DETSNOW in January, respectively. As already discussed, FALLOUT and DETSNOW enhance large-scale cloud microphysical processes relative to FALLIN by increasing convective detrainment between EAUCUP and EAULIQ. Increased moistening of the tropical middle-troposphere between DETSNOW and FALLOUT, and DETSNOW and FALLIN is well seen in Fig. 17a. Difference plots of the zonally averaged temperature reveal a warmer tropical troposphere and colder extratropical troposphere in FALLOUT and FALLIN relative to DETSNOW, as seen in the middle and bottom panels of Fig. 17b. As expected, the increased temperature gradient between tropical and extratropical latitudes leads to stronger jet streams in both hemispheres, in conjunction with weaker upper-tropospheric westerlies in the Tropics, as seen in Fig. 17c. The intensity of the simulated zonal wind remains too strong when compared against ECMWF data.

We argue that the difference in the climate response of the CSU GCM in DETSNOW and in FALLIN results because of the difference in timescale between the parameterizations of convection and large-scale condensation. In FALLIN, the simulated climate locks itself into a warm and dry mode because the amount of condensed water and ice that EAUCUP converts to convective precipitation is initially instantaneously removed from the atmosphere. The amount of detrained cloud water and cloud ice provided to EAULIQ is small, reducing not only evaporation of large-scale cloud water and cloud ice, but also evaporation of falling rain and snow. Here, it is important to recall that unlike convective precipitation, precipitation simulated in EAULIQ is time-stepped explicitly (Fowler et al. 1996), providing opportunities for evaporation as it falls through subsaturated layers. In contrast, it is easier to maintain a colder and wetter atmosphere in DETSNOW than in FALLIN. In DETSNOW, less convective precipitation is initially instantaneously removed from the atmosphere because convective snow is removed at the tops of cumulus clouds, and more condensate is available to various cloud microphysical processes in EAULIQ. On monthly timescales, the more stable climate simulated in FALLIN yields lesser convective heating and drying, as seen in Figs. 12 and 13.

As discussed earlier, we did not attempt to tune EAUCUP, EAULIQ, or our parameterization of clouds and radiation in DETSNOW, which we use as our control simulation. As a result, the simulated globally averaged earth radiation budget and cloudiness are in significant disagreement with observations (Kiehl and Trenberth 1997; Schiffer and Rossow 1983), as shown in Table 2. Comparisons between the temperature simulated by the CSU GCM against that obtained with ECMWF reanalysis data showed that the simulated upper troposphere and stratosphere were systematically too cold and the simulated troposphere was systematically too warm, when compared against observations (Fowler and Randall 1996). In accordance with the difference between the simulated and observed meridional temperature gradient, the simulated climate had an unrealistically strong westerly jet in the winter hemisphere and subtropical

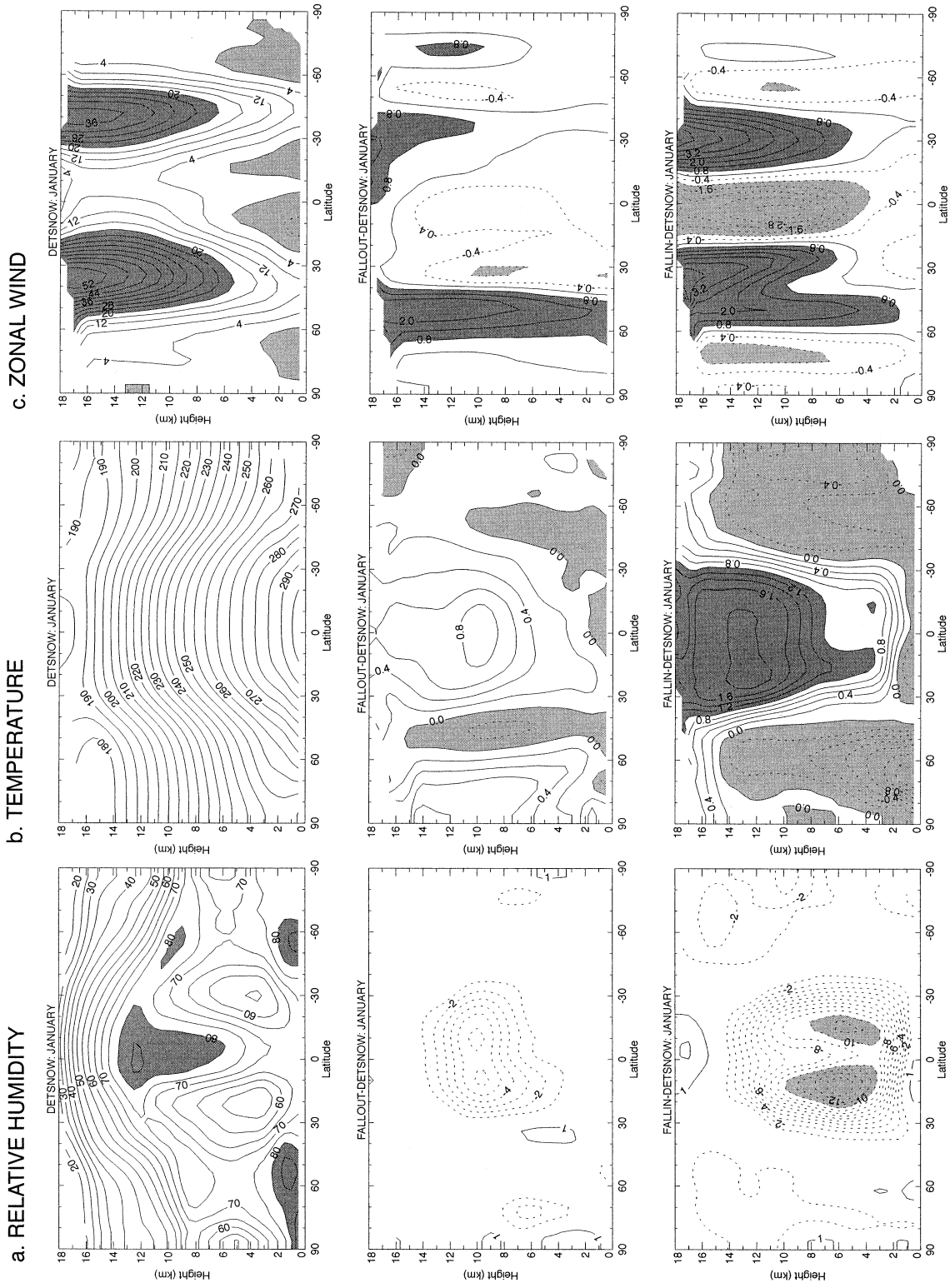

FIG. 17. Latitude–height cross sections of the zonally averaged atmospheric variables simulated by DETSNOW (top panels), and the differences in the zonally averaged atmospheric variables between FALLOUT and DETSNOW (middle panels), and FALLIN and DETSNOW (bottom panels): (a) relative humidity in percent, (b) temperature in kelvins, and (c) zonal wind in meters per second.

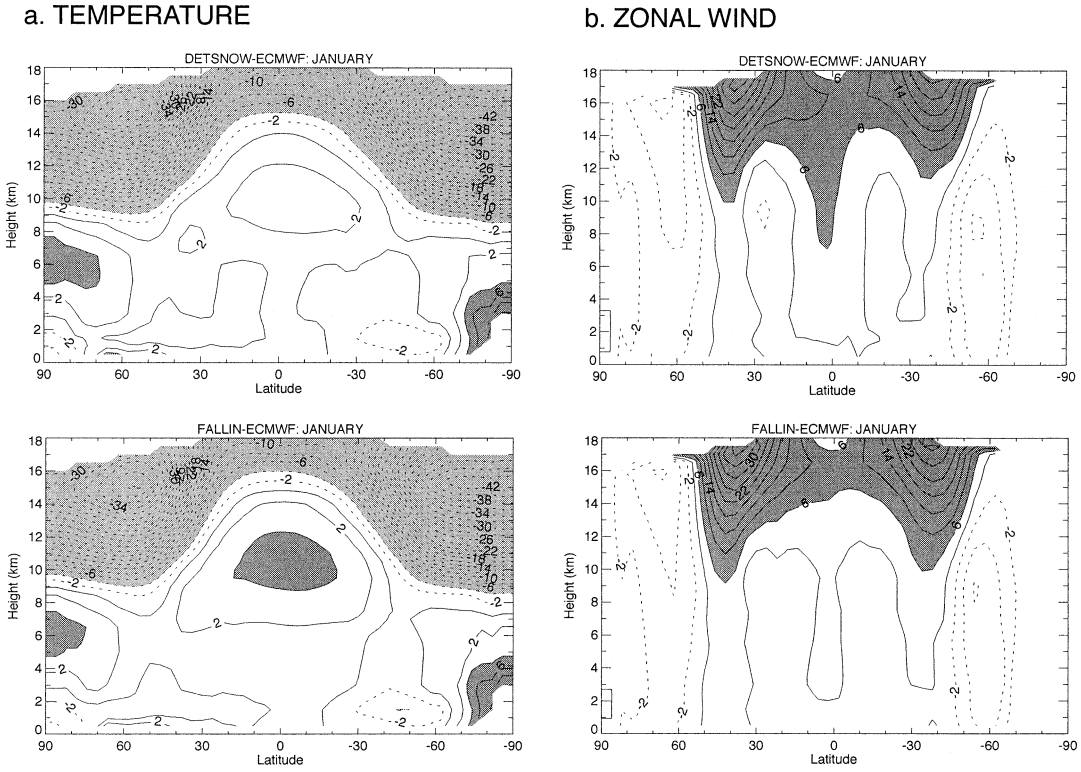

FIG. 18. Latitude–height cross sections of differences in the zonally averaged (a) temperature and (b) zonal wind. Top panels show differences between DETSNOW and ECMWF data, while bottom panels show differences between FALLIN and ECMWF data.

jet in the summer hemisphere. Similar comparisons between the zonal-mean temperature simulated in DETSNOW and ECMWF data would show a significant decrease of the tropospheric warm bias. The intensities of the westerly and subtropical jets are strongly reduced.

8. Summary

The inclusion of improved cloud microphysics and precipitation processes in parameterizations of convection is a key ingredient to improve interactions between convective and large-scale processes, especially through the formation of large-scale anvils by cumulus detrainment. In EAUCUP, we have taken a first step towards improving the simulated interactions between large-scale and convective processes by letting large-scale cloud water and cloud ice be entrained into the convective updrafts. Compensating subsidence of the large-scale cloud water, cloud ice, and snow is included in the computation of the convective tendencies. We have also taken a first step toward improving precipitation processes by allowing a fraction of the cloud ice formed in the convective updrafts to become snow, instead of letting all cloud ice be completely detrained at cloud tops. Furthermore, we investigated how the treatment of snow modifies the climate of the CSU GCM by allowing snow to be detrained at cloud tops, or instantaneously fall inside or outside the convective updrafts.

Unifying our parameterizations of large-scale cloud microphysics and convection through the entrainment of large-scale cloud water and cloud ice inside the updrafts, and large-scale compensating subsidence outside of the updrafts revealed to not be as important as originally hypothesized. Results of two separate sensitivity experiments designed to study these effects showed no significant differences in the simulated climate when compared to DETSNOW. These results were not discussed for brevity.

Our results support the conclusions of Emanuel and Pierrehumbert (1996) and Emanuel and Zivkovic-Rothman (1999) that cumulus convection schemes used in climate models need to describe in greater detail the microphysics of precipitation formation, especially for the cold phase. Differences in the zonally averaged temperature and relative humidity between FALLOUT and DETSNOW, and between FALLIN and DETSNOW stress the importance of correctly parameterizing the fraction of condensed water that precipitates or detrains at the tops of the clouds. Our main results show that the climate simulated by the CSU GCM is highly sensitive to the treatment of precipitation for the ice phase. A decrease in convective precipitation (but not neces-

sarily a decrease in convective activity) produces a moister but colder climate, as in DETSNOW. We argue that timescale differences between our parameterizations of convection and large-scale condensation, and the amount of condensate detrained at the tops of the updrafts relative to the amount that precipitates to the surface instantaneously explain most of the differences between FALLIN and DETSNOW.

Using EAUCUP as starting point, several avenues of research can be investigated. In particular, improved interactions between large-scale and convective processes through the entrainment of large-scale water vapor, cloud water, and cloud ice inside the convective updrafts, and compensating large-scale subsidence, are one of the key ingredients of our parameterization of fractional cloudiness (EAULIQNG; Randall and Fowler 1999). Entrainment of large-scale cloud water and cloud ice into a convective updraft simulates a mass exchange between a stratiform and convective cloud inside a model grid box. Upgrading our current parameterization of large-scale cloud microphysics (EAULIQ) with one that includes a prognostic equation for the horizontal cloud fraction (EAULIQNG) will help bring the simulated TOA outgoing longwave radiation and planetary albedo closer to their observed values. When local instead of grid-mean values are used, cloud water and cloud ice are converted more rapidly to rain and snow (Fowler and Randall 1996), and the cloud water and cloud ice paths simulated by the CSU GCM will change. Because the optical depth and infrared emissivity of stratiform clouds are functions of the local cloud water and cloud ice paths (Fowler and Randall 1996), we expect the optical properties of clouds, and hence the TOA to change also, especially in DETSNOW.

Acknowledgments. The TRMM data were provided by the NASA Goddard Space Flight Center Data Archive and Acquisition Center. This research was sponsored by the National Science Foundation under Grant ATM-9812384, the NASA Tropical Rainfall Measuring Mission (TRMM) under Grant NAG5-4749, and the Atmospheric Radiation Measurement (ARM) program under Grant DE-FG03-95ER61968. We want to thank three anonymous reviewers for their constructive criticism of the initial version of this manuscript.

REFERENCES

Anagostou, E. N., and C. Kummerow, 1997: Stratiform and convective classification of rainfall using SSM/I 85-GHz brightness temperature observations. *J. Atmos. Oceanic Technol.,* **14,** 570–575.

Arakawa, A., and W. H. Schubert, 1974: The interactions of a cumulus cloud ensemble with the large-scale environment. *J. Atmos. Sci.,* **31,** 674–701.

——, and K.-M. Xu, 1992: The macroscopic behavior of simulated convection and semiprognostic tests of the Arakawa–Schubert cumulus parameterization. *Physical Processes in Atmospheric Models,* D. R. Sikka and S. S. Singh, Eds., John Wiley and Sons, 3–18.

Betts, A. K., and M. J. Miller, 1986: A new convective adjustment scheme. Part II: Single column tests using GATE wave, BOMEX, ATEX, and arctic air-mass data sets. *Quart. J. Roy. Meteor. Soc.,* **112,** 693–709.

Cheng, M.-D., and A. Arakawa, 1997: Inclusion of rainwater budget and convective downdrafts in the Arakawa–Schubert cumulus parameterization. *J. Atmos. Sci.,* **54,** 1359–1378.

Del Genio, A. D., M.-S. Yao, W. Kovari, and K. K.-W. Lo, 1996: A prognostic cloud water parameterization for global climate models. *J. Climate,* **9,** 270–304.

Ding, P., 1995: A parameterization of cumulus convection with multiple cloud base levels. Ph.D. dissertation, Colorado State University, 235 pp.

——, and D. A. Randall, 1998: A cumulus parameterization with multiple cloud bases. *J. Geophys. Res.,* **103,** 11 341–11 353.

Donner, L. J., C. J. Seman, and R. S. Hemler, 2001: A cumulus parameterization including mass fluxes, convective vertical velocities, and mesoscale effects: Thermodynamic and hydrological aspects in a general circulation model. *J. Climate,* **14,** 3444–3463.

Emanuel, K. A., and R. T. Pierrehumbert, 1996: Microphysical and dynamical control of tropospheric water vapor. *Clouds, Chemistry, and Climate,* P. J. Crutzen and V. Ramanathan, Eds., Springer-Verlag, 264 pp.

——, and M. Zivkovic-Rothman, 1999: Development and evaluation of a convection scheme for use in climate models. *J. Atmos. Sci.,* **56,** 1766–1782.

Fowler, L. D., and D. A. Randall, 1996: Liquid and ice cloud microphysics in the CSU general circulation model. Part II: Impact on cloudiness, the earth's radiation budget, and the general circulation of the atmosphere. *J. Climate,* **9,** 530–560.

——, and ——, 2000: EAUliq NG: The second generation of cloud microphysics and fractional cloudiness in the CSU general circulation model. *Proc. 13th Int. Conf. on Clouds and Precipitation,* Reno, NV, ICCP, 444–445.

——, ——, and S. A. Rutledge, 1996: Liquid and ice cloud microphysics in the CSU general circulation model. Part I: Model description and simulated cloud microphysical processes. *J. Climate,* **9,** 489–529.

Harshvardhan, D. A. Randall, T. G. Corsetti, and D. A. Dazlich, 1989: Earth radiation budget and cloudiness simulated with a general circulation model. *J. Atmos. Sci.,* **46,** 1922–1942.

Hong, Y., C. D. Kummerow, and W. S. Olson, 1999: Separation of convective and stratiform precipitation using microwave brightness temperatures. *J. Appl. Meteor.,* **38,** 1195–1213.

Houze, R. A., Jr., 1997: Stratiform precipitation in regions of convection: A meteorological paradox? *Bull. Amer. Meteor. Soc.,* **78,** 2179–2196.

Jakob, C., 2000: The representation of cloud cover in atmospheric general circulation models. Ph.D. dissertation, Dept. of Physics, Ludwig-Maximillians University, Munich, Germany, 194 pp.

Kiehl, J. T., and K. E. Trenberth, 1997: Earth's annual global mean energy budget. *Bull. Amer. Meteor. Soc.,* **78,** 197–208.

Kummerow, C., W. Barnes, T. Kozu, J. Shiue, and J. Simpson, 1998: The Tropical Rainfall Measuring Mission (TRMM) sensor package. *J. Atmos. Oceanic Technol.,* **15,** 809–817.

Lin, X., D. A. Randall, and L. D. Fowler, 2000: Diurnal variability of the hydrological cycle and radiative fluxes: Comparisons between observations and a GCM. *J. Climate,* **13,** 4159–4179.

Lord, S. J., 1978: Development and observational verification of a cumulus cloud parameterization. Ph.D. dissertation, University of California, Los Angeles, 359 pp.

——, W. C. Chao, and A. Arakawa, 1982: Interactions of a cumulus ensemble with the large-scale environment. Part IV: The discrete model. *J. Atmos. Sci.,* **39,** 104–113.

Moorthi, S., and M. J. Suarez, 1992: Relaxed Arakawa–Schubert: A parameterization of moist convection for general circulation models. *Mon. Wea. Rev.,* **120,** 978–1002.

Pan, D.-M., 1995: Development and application of a prognostic cu-

mulus parameterization. Ph.D. dissertation, Colorado State University, 207 pp.
——, and D. A. Randall, 1998: A cumulus parameterization with a prognostic closure. *Quart. J. Roy. Meteor. Soc.*, **124,** 949–981.
Randall, D. A., and D. G. Cripe, 1999: Alternative methods for specification of observed forcing in single-column models and cloud system models. *J. Geophys. Res.*, **104,** 24 527–24 545.
——, and L. D. Fowler, 1999: EAUliq: The next generation. Atmospheric Science Paper 673, Department of Atmospheric Science, Colorado State University, 65 pp.
——, K.-M. Xu, R. J. C. Sommerville, and S. Iacobellis, 1996: Single-column models and cloud ensemble models as links between observations and climate models. *J. Climate*, **9,** 1683–1697.
Randel, D. L., T. H. Vonder Haar, M. A. Ringerud, G. L. Stephens, T. J. Greenwald, and C. L. Combs, 1996: A new water vapor dataset. *Bull. Amer. Meteor. Soc.*, **77,** 1233–1246.
Rasch, P. J., and J. E. Kristjansson, 1998: A comparison of the CCM3 climate model using diagnosed and predicted condensate parameterizations. *J. Climate*, **11,** 1587–1614.
Renno, N. O., K. A. Emmanuel, and P. H. Stone, 1994: Radiative–convective model with an explicit hydrological cycle. 1: Formulation and sensitivity to model parameters. *J. Geophys. Res.*, **99,** 14 429–14 441.
Rosenfeld, D., E. Amitai, and D. B. Wolff, 1995: Classification of rain regimes by the three-dimensional properties of reflectivity fields. *J. Appl. Meteor.*, **34,** 198–211.
Rotstayn, L. D., 1997: A physically based scheme for the treatment of stratiform clouds and precipitation in large-scale models. I: Description and evaluation of the microphysical processes. *Quart. J. Roy. Meteor. Soc.*, **123,** 1227–1282.
Schiffer, R., and W. B. Rossow, 1983: The International Satellite Cloud Climatology Project (ISCCP): The first project of the World Climate Research Program. *Bull. Amer. Meteor. Soc.*, **64,** 779–784.
Simpson, J., C. Kummerow, W.-K. Tao, and R. F. Adler, 1996: On the Tropical Rainfall Measuring Mission (TRMM). *Meteor. Atmos. Phys.*, **60,** 19–36.
Steiner, M., and S. E. Yuter, 1995: Climatological classification of three-dimensional storm structure from operational radar and rain gauge data. *J. Appl. Meteor.*, **34,** 1978–2007.
Stokes, G. M., and S. E. Schwartz, 1994: The Atmospheric Radiation Measurement (ARM) Program: Programmatic background and design of the cloud and radiation test bed. *Bull. Amer. Meteor. Soc.*, **75,** 1201–1221.
Suarez, M. J., A. Arakawa, and D. A. Randall, 1983: Parameterization of the planetary boundary layer in the UCLA general circulation model: Formulation and results. *Mon. Wea. Rev.*, **111,** 2224–2243.
Sud, Y. C., and G. K. Walker, 1999a: Microphysics of clouds with the relaxed Arakawa–Schubert scheme (McRAS). Part I: Design and evaluation with GATE Phase III data. *J. Atmos. Sci.*, **56,** 3196–3220.
——, and ——, 1999b: Microphysics of clouds with the relaxed Arakawa–Schubert scheme (McRAS). Part II: Implementation and performance in GEOS II GCM. *J. Atmos. Sci.*, **56,** 3221–3240.
Tiedtke, M., 1993: Representation of clouds in large-scale models. *Mon. Wea. Rev.*, **121,** 3040–3061.